An ancestral dual function of OmpM as outer membrane tether and nutrient uptake channel in diderm Firmicutes

Augustinas Silale, Yiling Zhu, Jerzy Witwinowski, Robert Smith, Kahlan Newman, Satya Bhamidimarri, Arnaud Baslé, Syma Khalid, Christophe Beloin, Simonetta Gribaldo, et al.

Dual function of OmpM as outer membrane tether and nutrient uptake channel in diderm Firmicutes

Augustinas Silale[1], Yiling Zhu[1], Jerzy Witwinowski[2], Robert E. Smith[2], Kahlan E. Newman[3], Satya P. Bhamidimarri[1], Arnaud Baslé[1], Syma Khalid[4], Christophe Beloin[5*], Simonetta Gribaldo[2*], Bert van den Berg[1*]

[1] Biosciences Institute, Faculty of Medical Sciences, Newcastle University, Framlington Place, NE2 4HH, Newcastle upon Tyne, UK

[2] Institut Pasteur, Université de Paris Cité, UMR CNRS 6047, Unit Evolutionary Biology of the Microbial Cell, Paris, France

[3] School of Chemistry, University of Southampton, Southampton, SO17 1BJ, UK

[4] Department of Biochemistry, University of Oxford, Oxford, OX1 3QU, UK

[5] Institut Pasteur, Université de Paris Cité, UMR CNRS 6047, Genetics of Biofilms Laboratory, Paris, France

* Correspondence to: bert.van-den-berg@newcastle.ac.uk;
simonetta.gribaldo@pasteur.fr
christophe.beloin@pasteur.fr

Abstract

The outer membrane (OM) in diderm, or Gram-negative, bacteria must be tethered to peptidoglycan for mechanical stability and to maintain cell morphology. Most diderm phyla from the Terrabacteria group have recently been shown to lack well-characterised OM attachment systems, but instead have OmpM, which could represent an ancestral tethering system in Bacteria. Here, we have determined the structure of the most abundant OmpM protein from *Veillonella parvula* (diderm Firmicutes) by single particle cryo- electron microscopy. We also characterised the channel properties of the transmembrane β-barrel of OmpM and investigated the structure and PG-binding properties of its periplasmic stalk region. Our results show that OM tethering and nutrient acquisition are genetically linked in *V. parvula,* and probably other diderm Terrabacteria. This dual function of OmpM may have played a role in the loss of the OM in ancestral bacteria and the emergence of monoderm bacterial lineages.

Introduction

The defining feature of diderm, or Gram-negative, bacteria is the presence of an outer membrane (OM)[1,2]. This complex cell envelope component is an asymmetric lipid bilayer, usually containing lipopolysaccharide (LPS) in the outer leaflet and phospholipids in the inner leaflet. The first formal definition of an OM was subsequent to an electron microscopy analysis of the cell envelope of the diderm Firmicute *Veillonella parvula* (Negativicutes class)[3]. However, most of our knowledge about the OM derives from studies of Proteobacteria, especially *Escherichia coli*. While the OM provides mechanical stabilisation to the cell[4], diderm bacteria must tether the OM to peptidoglycan (PG) for additional mechanical stability and to maintain cell morphology. *E. coli* has three OM tethering systems: Braun's lipoprotein (Lpp) that covalently links the PG with the OM[5,6], the lipoprotein Pal and the OM protein OmpA which associate with PG non-covalently[7–11]. Mutants of these systems exhibit cell envelope defects and increased susceptibility to cell envelope stressors, such as detergents[7,12–15].

Recent phylogenetic analysis of the distribution of OM attachment systems throughout the Bacteria Tree of Life has highlighted a striking bimodal distribution across the two major clades in which Bacteria are divided, the Terrabacteria (including both classical monoderms such as Bacilli and Clostridia, and diderms such as Cyanobacteria and Deinococcus-Thermus) and the Gracilicutes (including only diderms such as Proteobacteria and Bacteroidetes)[16]. Braun's lipoprotein was shown to be only present in a subset of Proteobacteria, and Pal restricted to the Gracilicutes, together with the Lol machinery for lipoprotein export to the OM. OmpA showed a patchy distribution, being absent in many diderms. In contrast, the OmpM protein is a fourth OM tethering

68 system that appears to be widespread in diderm Terrabacteria but is completely
69 absent in the Gracilicutes[16].
70
71 OmpM consists of an N-terminal periplasmic S-layer homology (SLH) domain
72 connected via a linker region to a C-terminal OM β-barrel[17–20]. The SLH domain has
73 been mostly studied for its role in the building of S-layers in monoderm bacteria[21]. The
74 primary role of the SLH domain is binding to the cell wall. Similarly to the SLH domain
75 found in monoderm S-layer proteins[22–24], the SLH domain of OmpM proteins of some
76 diderm Terrabacteria phyla such as Thermus and Cyanobacteria has been shown *in*
77 *vitro* to bind pyruvylated secondary cell wall polymers (SCWPs)[25–27], whereas in
78 members of the Negativicutes (including *V. parvula*) it anchors the OM to PG modified
79 with polyamines (e.g. cadaverine and putrescine) on the D-glutamate of the peptide
80 stem[18,28,29].
81
82 Deletion of three out of the four OmpM paralogues in *V. parvula* resulted in a dramatic
83 phenotype where the OM detaches, the periplasmic space is greatly enlarged and
84 multiple cells share a single OM[16]. Complementation by the most abundant *V. parvula*
85 OmpM paralogue, OmpM1, reverted this phenotype back to wild type, demonstrating
86 *in vivo* that OmpM is responsible for tethering the OM to PG[16]. This dramatic
87 phenotype after deletion of OmpM-like proteins has been reported also in two other
88 representatives of diderm Terrabacteria, *Thermus aquaticus*[30] and *Deinoccoccus*
89 *radiodurans*[31,32].
90
91 These results led to the proposal that OmpM proteins represent an ancestral OM
92 tethering system in Terrabacteria and possibly the last bacterial common ancestor,

93 which united anchoring and nutrient acquisition functions[16]. The presence of this
94 unique OM tether in Terrabacteria might therefore have been involved in the multiple
95 OM-loss events inferred to have occurred specifically in this clade, perhaps via OmpM
96 mutations weakening (and eventually abolishing) the SLH-PG interactions[16].
97
98 Due to its LPS component, the OM presents a permeability barrier for hydrophilic and
99 hydrophobic small molecules, both detrimental (*e.g*. antibiotics) and essential (*e.g*.
100 nutrients)[33,34]. Controlled permeability of the OM is established by OM proteins, which
101 either mediate energized transport of specific nutrients in the case of TonB-dependent
102 transporters, or allow size-limited diffusion in the case of porins (<~600 Da for rigid
103 spherical molecules[33,34], although larger flexible molecules can also go through[35]).
104 Porins are well-characterised in many Proteobacteria, but much less information is
105 available on small-molecule permeation in diderm Terrabacteria. Earlier work on the
106 OmpM-like protein Mep45 from the Negativicute *Selenomonas ruminantium*
107 suggested that this protein can transport nutrients via its β-barrel domain[19], but
108 another study in *Synechocystis* (Cyanobacteria) claimed that its OmpM orthologues
109 form channels too small for most simple nutrients[20]. In *V. parvula,* the role of OmpM
110 in nutrient acquisition has not been studied. In addition to the four OmpM paralogues,
111 there are two other putative porin genes in the *V. parvula* genome: an OmpA-like
112 homologue (*FNLLGLLA_00518*) and a porin (*FNLLGLLA_00833*)[36]. Proteomic
113 analysis of the *V. parvula* OM showed that OmpM1, OmpM2 and FNLLGLLA_00833
114 are, respectively, the first, third, and sixth most abundant OM proteins[36], suggesting
115 that these proteins could play major roles in determining OM permeability.
116

A recent analysis has proposed that the barrels of most OmpM-like proteins have 16-30 β–strands[37], and could therefore form pores that are large enough for small molecule diffusion across the OM, a hypothesis supported by electrophysiology experiments with *Deinococcus radiodurans* SlpA protein[38] and liposome swelling studies on Mep45 from *S. ruminantium*[19]. The recently determined structures of SlpA revealed that it forms a large trimeric complex composed of 30-stranded β-barrels, *i.e*. much larger than those of the general *E. coli* porins OmpC and OmpF[37,39]. However, since *D. radiodurans* has an unusually complex cell envelope with an S-layer[31,40,41], it is unclear how generalisable these findings are to OmpM proteins in other diderm Terrabacteria, especially in Negativicutes which tether the OM to polyaminated PG rather than pyruvylated SCWP.

Here we use single particle cryo-EM, X-ray crystallography, molecular dynamics simulations, bioinformatic analyses and functional assays to show that OmpM1 from *V. parvula* (VpOmpM1) is a general porin with similar structural and functional properties to *E. coli* OmpF, with an additional mobile periplasmic region that can bind *V. parvula* PG and take on different folds. We also show that the four OmpM paralogues are likely the only porins in *V. parvula*, implying that nutrient acquisition and OM attachment are genetically linked in diderm Firmicutes, and likely all diderm Terrabacteria, via OmpM. Our results support an ancestral dual function of OmpM as both an OM tether and nutrient uptake porin which may have supported life in early bacteria.

Results

VpOmpM1 is a trimeric porin with an extended periplasmic region

We determined the structure of VpOmpM1 expressed in *E. coli* by single particle cryo-EM (Figure 1a-d and Supplementary Table 1). Reconstructions up to 3.2 Å without enforced symmetry revealed a trimeric arrangement of the protomers. The C-terminal 16-stranded β-barrels that reside in the OM form a classical three-fold symmetrical porin assembly reminiscent of the well-characterised *E. coli* porins OmpF (EcOmpF) and OmpC[42,43]. However, the β-barrel lumens are constricted by inward-folded extracellular loops 3 and 7 in VpOmpM1 (Figure 1b), rather than solely by loop 3 as in the *E. coli* porins. The inter-protomer contact area, mediated by hydrophobic sidechains on the outside of the β-barrel, completely excludes lipid/detergent and solvent. The β-barrels exhibit other features common to known porin structures, including an aromatic girdle at the membrane-solvent interfaces and strong density surrounding the β-barrels that likely corresponds to the lipid moieties of LPS and phospholipid or detergent (Figure 1b, d and Supplementary Fig. 1). An unusual feature observed in the cryo-EM reconstructions was a weaker, elongated density that corresponds to the N-terminal SLH domain at the distal part, connected to the β-barrel via a triple coiled coil (Figure 1c, d). We term this periplasmic region of VpOmpM1 the 'stalk'. Only the region of the stalk proximal to the OM was resolved well enough for model building, as the cryo-EM density deteriorates towards the SLH domain end of the stalk. We speculated that the poor density is the result of movement of the stalk relative to the β-barrels. Measurements of the blurry SLH domain density observed in 2D class averages suggest that the distal part of the stalk spans 50-60 Å (Figure 1c). The VpOmpM1 trimer is pseudosymmetrical: while the β-barrels exhibit three-fold symmetry, the stalk is tilted relative to the membrane plane normal (Figure 1d). The

pseudosymmetry was confirmed by enforcing C3 symmetry during data processing, which resulted in a better-resolved β-barrel region (2.8 Å) but uninterpretable density for the periplasmic stalk (Supplementary Fig. 2-4).

The *E. coli* cell wall does not contain polyaminated PG, the native ligand of VpOmpM1. Therefore, to exclude the possibility that in our structure of VpOmpM1 purified from *E. coli* the stalk region is misfolded due to the absence of polyaminated PG, we purified a His-tagged OmpM1 construct expressed in *V. parvula* (native VpOmpM1) and determined its structure by single particle cryo-EM to 3.3 Å resolution (Supplementary Table 1, Supplementary Fig. 2-4). The β-barrel structures are virtually identical (Cα-Cα root-mean-square deviation 0.239 Å), but there are differences in the relative orientation of the stalk (Figure 1e). In reconstructions without enforced symmetry, the α-helices forming the coiled-coil are not equivalent in either dataset, as they exit the OM plane in different orientations (Figure 1f). The reasons for these structural differences are not obvious. We speculate that intra- or inter-protomer hydrogen bonds at the stalk-barrel interface could be responsible for the subtle conformational differences. In the *E. coli* VpOmpM1 structure, the sidechain of R113 in one protomer interacts with the sidechain of N155 (part of the periplasmic end of the β2 strand) of another protomer. This interaction is observed only in two inter-protomer interfaces, but not the third one (Figure 1g). A similar interaction was observed in the native VpOmpM1 structure: at two inter-protomer interfaces, R113 interacts with the carbonyl oxygen of G115 and the sidechain of N116 (both part of the β-barrel end of the stalk) (Figure 1h). Interestingly, the R113-N155 interaction was not observed in the native VpOmpM1 structure, and the R113-G115/N116 interaction was not observed in the

VpOmpM1 structure from *E. coli*. It is possible that the two protein constructs differ slightly in their lowest energy states which are observed in the averaged cryo-EM data.

We performed all-atom molecular dynamics (MD) simulations to investigate the conformational space sampled by the stalk. We simulated the native VpOmpM1 model to which an AlphaFold2[45] prediction of the unmodeled region of the stalk was grafted and fit into the low resolution cryo-EM density (Figure 2a). The simulations revealed substantial movement of the stalk in the periplasmic space (Supplementary Movie 1). The SLH domain end of the stalk sampled a span of ~50 Å (Figure 2b) during the simulations, in agreement with the cryo-EM data (Figure 1c). The coiled-coil does not kink throughout the 1 μs simulation (Figure 2c), and the movement of the stalk is due to flexibility at the interface between the stalk and the β-barrels. We observed that the inter-protomer hydrogen bonds identified in our static cryo-EM structures, R113-N155 and R113-G115, are broken and re-formed throughout the simulation (Figure 2d). The R113 interaction with the sidechain of N116 was not stable, and R113 instead interacted with the backbone carbonyl oxygen of N116 (Figure 2d). Similar results were obtained from a replicate simulation with the AlphaFold2 graft model as well as the native VpOmpM1 cryo-EM model by itself (Supplementary Fig. 5). The stalk would presumably be bound to the relatively immobile PG in vivo, which would significantly impair its mobility relative to the OM. We speculate that the flexible interface between the stalk and the β-barrels would result in the ability of the OM to move slightly relative to the PG, imparting mechanical resistance to the cell envelope.

The stalk binds polyaminated peptidoglycan

The SLH domain of OmpM binds polyaminated PG *in vivo*, as demonstrated in the Negativicute *S. ruminantium*[18,28]. Recent evidence for VpOmpM1 binding to PG comes from fluorescence microscopy and cryogenic electron tomography experiments that showed OM detachment when three *ompM* paralogues were deleted[16]. We tested binding of recombinant full-length and barrel-only VpOmpM1 to sacculi isolated from *V. parvula* and *E. coli* (Figure 3a). Only full-length protein binds to *V. parvula* sacculi, as expected. Minor amounts of full-length VpOmpM1 were found in the wash fraction, suggesting that the non-covalent PG-SLH domain interaction is reasonably strong. No binding was observed to sacculi from *E. coli,* confirming that PG stem peptide polyamination is required for binding.

The cryo-EM density for VpOmpM1 SLH domains was not sufficiently resolved for model building due to movement of the stalk, as demonstrated by MD simulations. We therefore used bioinformatics and structural comparisons to investigate where polyaminated PG could bind within the AlphaFold2 predicted model of VpOmpM1 SLH domains. Monoderm bacteria attach cell surface proteins to SCWPs using single-chain proteins that have triple tandem SLH domain repeats, which fold into a core three α-helix bundle with additional helices and loops packing against this bundle[22,46–49]. Available crystal structures of the SLH domains 1-3 of *Bacillus anthracis* surface array protein (Sap) and *Paenibacillus alvei* S-layer protein SpaA are similar to the predicted VpOmpM1 SLH domain[46,47] (Figure 3b) with Cα-Cα r.m.s.d values of 1.0 and 1.3 Å, respectively. The main difference is that both Sap and SpaA have short core helical bundles, but the VpOmpM1 central bundle extends into the long coiled-coil that connects it to the β-barrels. Structures of SpaA bound to defined SCWP ligands[47] show that the sugars bind in grooves between SLH repeats (Figure 3b) and

239 interact with conserved motifs therein: conserved tryptophan and glycine residues bind
240 the sugar moiety (W34 and G58 in VpOmpM1), and the arginine of the TRAE motif
241 forms a salt bridge with the ketal-pyruvate modification of the SCWP (residues 63-66,
242 TRYE, in VpOmpM1). It is not surprising that these motifs are conserved in most
243 OmpM-like proteins from diderm Terrabacteria because they are thought to bind
244 pyruvylated SCWP, but not in the Negativicutes (Figure 3c).
245
246 Negativicute OmpM proteins are thought to recognise the polyamine modification on
247 the α-carboxylate of the D-glutamate in the PG peptide stem. Crystal structures of
248 proteins bound to putrescine[50–52] and cadaverine[53,54] indicate that aromatic residues
249 are involved in binding these polyamines via stacking interactions with the aliphatic
250 chain of the polyamine. We next investigated if the SLH domains are different between
251 OmpM and non-OmpM proteins (Figure 3c). We found that the tyrosine residue Y36
252 is highly conserved in the OmpM SLH domains from the Negativicutes and slightly
253 less in the other two lineages of diderm Firmicutes (Limnochordia and
254 Halanaerobiales), but it is not conserved in the SLH domains of OmpM homologues
255 from other diderm Terrabacteria as well as non-OmpM SLH domains (Figure 3c and
256 d). Also, Y65 of the TRYE motif is more conserved in the OmpM SLH domain of
257 Negativicutes than in the other groups of sequences.
258
259 Mapping these residues onto the predicted VpOmpM1 SLH domain structure reveals
260 that the conserved tyrosines are located away from the grooves between the SLH
261 chains that contain the putative PG disaccharide binding site (Figure 3e). We suggest
262 that the peptide stem containing the polyamine moiety specifically in Negativicutes
263 OmpM could extend away from the disaccharide binding groove to interact with either

of the conserved tyrosines. Alternatively, or perhaps additionally, PG interaction could induce conformational changes that bring the tyrosine side chains closer to the binding groove.

The stalk domain of OmpM may exist in compact and extended conformations

We generated a soluble construct encompassing almost the entire VpOmpM1 stalk region (residues 22-107) in *E. coli* and determined its crystal structure to 1.7 Å (Figure 4a, Supplementary Table 2, PDB 8BZ2) in an attempt to verify the AlphaFold2 prediction for this region. Surprisingly, the crystallized stalk does not fold into a coiled-coil but forms a compact trimer composed mainly of α-helices (residues 23-105). The protomer interfaces form grooves on one side of the trimer that could potentially accommodate ligands (Figure 4b). However, mapping of the previously identified putative PG-binding residues onto the stalk crystal structure shows they are spread across the structure (Supplementary Fig. 6), suggesting that this conformation does not bind PG. The residues that form the coiled-coil in the extended AlphaFold2 prediction instead form helical hairpins and extensive intra-protomer interactions rather than interact with the other chains in the asymmetric unit (Figure 4c). We obtained a very similar structure, albeit at a lower resolution, with a longer construct that encompasses the entire stalk region (residues 22-118). A DALI[56] search of the PDB using the SLH model (PDB 8BZ2) showed that it has low structural similarity to other proteins in the database (Supplementary Figure 5). The highest ranking hit was a blood group antigen binding adhesin (PDB 5F7L[57]) with a 5.7 Z-score and 2.5 Å Cα-Cα RMSD.

The protomer fold of the stalk observed in the crystal structures aligns well with an alternative, compact conformation predicted by AlphaFold2 (Figure 4d and e, Supplementary Fig. 8). This was surprising as the confidence for this prediction was low, yet it agreed with the experimental structure. However, the trimerization interface in the compact stalk prediction is different: residues that are far away in the crystal structure (e.g., M75) interact in the predicted compact conformation (Figure 3e). We considered that this compact state could be an unstable high energy conformation (hence the low prediction confidence), and that the stalk construct is stabilized in a similar conformation in the crystallization condition. Notably, the soluble SLH domain did not bind to *V. parvula* or *E. coli* sacculi (Figure 4f), unlike the full-length VpOmpM1 (Figure 3a). This suggests that the structure of the isolated SLH domain is different than in the full-length protein, as observed by cryo-EM. Therefore, we do not believe that the conformation observed in the crystal structure is the result of crystal packing.

All-atom MD simulation of VpOmpM1 with the compact stalk showed the stalk helix of one protomer reaching towards the OM, partially occluding the β-barrel of another protomer and forming salt bridges with its periplasmic turns (Figure 4g and Supplementary Movie 2). Additionally, this conformation was stabilised by inter-protomer hydrogen bonds in the stalk region (Supplementary Fig. 9). The role of this interaction is unclear, but this simulation supports the dynamic nature of the stalk.

The two different stalk conformations of VpOmpM1 imply that either there is conformational switching under the appropriate conditions (e.g., cell envelope stress, presence of specific ligands), or that the protein commits to a particular conformation during biogenesis. In one replicate of the all-atom MD simulations of the native

VpOmpM1-AlphaFold2 graft model (Figure 2a) we observed unfolding of the very N-terminus of the SLH domain of one chain, which then proceeded to interact with residues of the coiled-coil (Supplementary Movie 3, Supplementary Fig. 10). This suggests some flexibility for the SLH domain, and perhaps *in vivo* this flexibility is important for the SLH domain to find its PG ligand. The coiled-coil, however, remained stable during the simulation. Protein melting temperature analysis by dynamic scanning calorimetry suggested that the melting temperature of the stalk in the full-length VpOmpM1 construct is ~87˚C (Supplementary Fig. 11), which means that the coiled-coil interaction is very stable and it is unlikely to unfold under physiological conditions. Therefore, the more favourable hypothesis is that the VpOmpM1 trimer is committed to either the extended or compact stalk conformation during biogenesis.

OmpM paralogues are the only general diffusion porins in *V. parvula*

The β-barrel of VpOmpM1 consists of 16 anti-parallel β-strands connected by extracellular loops and periplasmic turns similar to the *E. coli* porin OmpF (Figure 1b,c). Although sequence similarity of VpOmpM1 to *Ec*OmpF is only 25%, the overall structure is similar, but with some prominent differences in the extracellular loops (Figure 5a and Supplementary Fig. 12). VpOmpM1 extracellular loops 3 and 7 fold into the β-barrel to form the constriction. In EcOmpF and similar Proteobacterial general porins the constriction is formed solely by loop 3 (Figure 5a). The eyelet (the narrowest region of the pore) is formed by sidechains projecting from the β-barrel strands into the lumen as well as sidechain and backbone atoms of the constricting loop residues (Figure 5b). Analysis of the pore radius of experimental structure β-barrels by the HOLE program[58] reveals a maximal constriction of ~3.7 Å (Figure 5c). However, in EcOmpF the extent of the constriction (± 0.1 Å) along the axis perpendicular to the

membrane plane is ~2.4 Å, and the VpOmpM1 constriction extends for ~7 Å. All-atom MD simulations show that the pore constriction in VpOmpM1 is constant due to an extensive interaction network restricting movement of the eyelet loops 3 and 7 (Supplementary Figure 13). In agreement with a previous report[59], we observed that this is not the case in EcOmpF, where fluctuations in loop 3 can completely close the pore.

An electric field exists across the eyelet of general porins as a result of asymmetric distribution of charged residues[60,61], and a similar charge asymmetry is seen in the eyelets of VpOmpM1 and EcOmpF (Figure 5b). We calculated the average dipole moment of water molecules inside the channel during the MD simulations and used this as a proxy for comparing the strength of the transverse electric field inside the two porins. The largest average dipole moment magnitudes are observed in the constriction regions (Supplementary Figure 14), and the direction of the dipole points from the acidic residues towards the basic residues of the eyelet. This analysis shows that the EcOmpF constriction has a stronger localised transverse electric field, while VpOmpM1 has a weaker and more diffuse transverse electric field.

We tested the ability of VpOmpM1 to transport small molecules across membranes in liposome swelling assays (Figure 6a). Notably, VpOmpM1 could transport lactate, which is essential for *V. parvula* growth, and putrescine, which is used for modification of the PG peptide stem. We also observed transport of the amino acids arginine, lysine, glutamate, aspartate, glycine, alanine, leucine, and methionine. VpOmpM1 transported monosaccharides, even though *V. parvula* is asaccharolytic, but not disaccharides, which underlines the non-specific, size-limited nature of transport. We

363 carried out experiments with a VpOmpM1 construct that lacks the stalk to test if the
364 stalk is involved in regulating transport, but this construct had similar transport
365 properties to the full-length protein (Figure 6a). The only exception was impaired
366 transport of arginine and alanine, and the reasons for this are unclear. VpOmpM1 had
367 a similar substrate permeation profile to EcOmpF but showed consistently lower
368 transport rates, which could be the consequence of a longer constriction region or
369 weaker transverse electric field (Figure 5c and Supplementary Figure 14). One notable
370 difference is that there was little transport of ampicillin, kanamycin and gentamicin by
371 VpOmpM1 compared to EcOmpF (Figure 6a), but the relevance of this for antibiotic
372 resistance *in vivo* is unclear.
373
374 We further characterised the channel properties of VpOmpM1 in bilayer
375 electrophysiology experiments. Initially, we obtained conductance value distributions
376 from recordings with multiple channel insertion events (Figure 6b and Supplementary
377 Fig. 15a,b). The resulting distributions were very broad and centred at 4.87 ± 1.86 nS
378 and 4.66 ± 1.88 nS for the full-length and barrel-only constructs of VpOmpM1,
379 respectively. The broad conductance distributions are likely due to multiple sub-
380 conductance states of the channel, as observed in recordings where the channels can
381 randomly close to different extent (Figure 6c and Supplementary Fig. 15c,d). We were
382 able to get more accurate conductance values from single channel recordings: 4.34 ±
383 0.46 nS (mean ± SD, n=8) for full-length VpOmpM1 and 4.37 ± 0.28 nS (mean ± SD,
384 n=8) for barrel-only VpOmpM1. In single channel recordings at higher voltages, we
385 occasionally observed classical trimeric porin behaviour where the three protomer
386 pores close sequentially (Figure 6c and Supplementary Fig. 15c,d). Using our setup
387 we obtained a conductance of 4.28 ± 0.19 (mean ± SD, n=9) for EcOmpF, which is

similar to previously reported values[62,63] and to VpOmpM1 conductance. Current-voltage characteristics for both VpOmpM1 constructs and EcOmpF were again very similar (Figure 6d).

We conclude that VpOmpM1 is a general diffusion channel in *V. parvula*, with similar properties to EcOmpF. We expect that the VpOmpM2-4 paralogues also function as nutrient uptake channels based on their sequence similarity[16]. We think it is unlikely that the other two putative porins of *V. parvula*, FNLLGLLA_00518 and FNLLGLLA_00833, also transport nutrients because they are predicted to only have 10 strands in their β-barrels (Figure 7a,b). Previous work on 10-stranded β-barrels has shown that their lumen is occluded by amino acid residue sidechains and that they cannot perform major transport roles[65,66]. To verify this experimentally, we produced the β-barrel region of FNLLGLLA_00518 in sufficient quantities for liposome swelling experiments. It did not transport lactate and arabinose, and could only transport putrescine and glycine at much slower rates than VpOmpM1 and EcOmpF (Figure 7c), in agreement with reported transport properties of small OM β-barrels[67,68]. Therefore, FNLLGLLA_00518 is not a general porin. We were not able to test the transport activity of FNLLGLLA_00833 because the protein could not be expressed in *E. coli*, but we expect this 10 β-strand OM protein to have very low substrate permeation rates as well.

Discussion

Together, our results show that OmpM has a dual function as an OM tethering system and a nutrient uptake channel. Our structures, simulations and functional data provide insight into how these key OM-related functions are linked in diderm Firmicutes and probably many other diderm Terrabacteria that possess OmpM-like attachment systems and lack the well-characterised tethers present in the Gracilicutes.

Interestingly, structural data and MD simulations show that the extended stalk of VpOmpM1 is highly mobile. The functional consequences of this mobility are not clear, and neither is it clear why it may be preferable to a rigid connection between the PG and OM. One possibility is that the stalk samples the local environment to find polyaminated-PG. Although one would expect the polyamine modification to be present on most peptide stems, PG spatial organization is not well understood, and it is unclear what proportion of the modified peptide stems is easily accessible to the SLH domains of VpOmpM1. Another possibility is that the flexible interface between the stalk and the β-barrels imparts favourable mechanical properties to the cell envelope, as having a somewhat flexible PG-OM tether would allow the OM to deform when external mechanical forces are applied.

The combination of structural, functional and bioinformatics data suggests the possibility that the stalk exists in multiple conformations, despite the fact we did not observe any particle populations with a compact stalk in our cryo-EM datasets. Unravelling the roles of both potential states of the stalk is a challenging problem that will likely have to be resolved using *in vivo* studies. Based on structural comparisons with SCWP-binding SLH domains from monoderm bacteria and our PG binding assay

results, we can conclude that the extended stalk state observed in cryo-EM reconstructions of VpOmpM1 is the PG-binding state.

The stalked OmpM-like porins represent a new variation of SLH domains. The three copies of the SLH domain from separate protein chains come together to form three likely identical ligand-binding sites, whereas previously characterised triple SLH domains are encoded in a single chain and their ligand-binding grooves have different affinities for SCWPs due to differences in binding motif residues in each SLH repeat[47,49,69,70]. The functional consequences of having equivalent or non-equivalent ligand binding sites are not clear in the context of protein anchoring to the PG/SCWP.

SlpA from *D. radiodurans* is the only other OmpM-like protein for which structures have been determined[37–39]. SlpA, like VpOmpM1, plays an important role in maintaining cell envelope integrity[16,31]. VpOmpM1 is similar to SlpA in its overall architecture: both proteins are trimers and have an N-terminal SLH domain connected via a coiled coil to a C-terminal β-barrel domain. However, the VpOmpM1 β-barrel trimer is approximately the size of a single SlpA β-barrel (Supplementary Fig. 16). Consequently, the pore inside the SlpA β-barrel, although constricted by extracellular loop insertions, is much larger than in VpOmpM1 and is ~14 Å in diameter at the narrowest point. VpOmM1 clearly imposes a size filter for diffusion across the OM (Figures 5 and 6) and prevents leakage of large periplasmic contents from the cell. SlpA has been shown to transport nutrients[38], but it is unclear how escape of periplasmic material via the massive SlpA β-barrel pore is prevented *in vivo*. Other components of the complex and unusual cell envelope characteristics of *D. radiodurans* could partially obstruct the SlpA pore[40,71]. A superoxide dismutase

460 (DR_0644) was observed bound at the top of the stalk and the β-barrel interface in
461 SlpA structures[37,39], and there are no homologues of this protein coded in the *V.*
462 *parvula* genome. The authors of one study noted that large (28-30 strand) β-barrels in
463 OmpM-like proteins appear to be confined to the Deinococcus-Thermus phylum[37].
464 Thus, the unusual β-barrel structure of SlpA and the superoxide dismutase partner
465 protein might be adaptations of this phylum to resist environmental extremes, such as
466 oxidative stress, radiation, vacuum conditions, and high temperatures[72].
467
468 VpOmpM1, on the other hand, could be more representative of OmpM proteins in
469 mesophilic diderm Terrabacteria. In fact, the β-barrel of Mep45, the OmpM homologue
470 from the Negativicute *S. ruminantium*, has been shown to form a diffusion channel
471 with similar properties to VpOmpM1, albeit with a larger estimated diameter (11.6 Å)
472 than that observed for VpOmpM1 (7.4 Å)[19]. Cyanobacterial OmpM homologues have
473 been shown to form small channels that facilitate transport of inorganic ions[20]. Our
474 VpOmpM1 structures suggest that OmpM homologues from these and perhaps most
475 diderm Terrabacteria might be similar to proteobacterial porins, unlike *D. radiodurans*
476 SlpA. Our results indeed show that nutrient acquisition and OM tethering are
477 genetically linked via OmpM in *V. parvula* and likely in all Negativicutes and other
478 diderm Terrabacteria.
479
480 In conclusion, these data support the recent hypothesis that OmpM is an ancestral
481 system that may have been present in the last common bacterial ancestor, possibly
482 consolidating two key OM-related functions, tethering and nutrient uptake[16].
483 Therefore, deletion of or mutations in *ompM* may have promoted loss of the OM due
484 to the concurrent loss of these fundamental cell functions. Although we envisage that

485 OmpM plays similar roles in all diderm Terrabacteria, experimental characterisation of
486 OmpM orthologues from diverse members of this clade will be required to fully capture
487 the conservation and variation of this ancient OM tethering system.

Methods

Bacterial strains, culture conditions and strain manipulation

Bacterial strains used in this work are listed in Supplementary Table 3. *E. coli* strains were genetically manipulated using standard laboratory procedures[73]. When needed, the following compounds were added to *E. coli* cultures at the following concentrations: ampicillin (liquid media) or ticarcillin (solid media) – 100 mg/l, chloramphenicol – 30 mg/l (liquid media) or 25 mg/l (solid media), kanamycin – 50 mg/ml, apramycin – 50 mg/l, diaminopimelic acid – 300 µM.

V. parvula was manipulated as described previously[16,74,75]. When needed, the following compounds were added to *V. parvula* cultures at the following concentrations: chloramphenicol – 25 mg/l, anhydrotetracycline – 250 µg/l. The anaerobic conditions were generated using the GenBag Anaer generator (Biomérieux), or the GP Campus anaerobic chamber (Jacomex). The anaerobic chamber was filled with a $H_2/CO_2/N_2$ (5%/5%/90%) mixture.

Plasmids, primers, and DNA manipulation

All plasmids and primers used in this study are listed in Supplementary Tables 4 and 5, respectively. Cloning was performed using either NEBuilder HiFi DNA Assembly Master Mix (New England Biolabs) or standard restriction cloning methods. Chemically competent *E. coli* DH5α or TOP10 cells[76] were used for transformation of cloning products or plasmids. *V. parvula* genomic DNA was extracted according to a protocol previously described for *Streptomyces* gDNA extraction[77] from stationary phase cultures in SK medium[78]. PCR reactions for cloning applications were carried out using Phusion HiFi Master Mix (Thermo Fisher Scientific) according to

manufacturer's protocol. PCR reactions for the control of constructs were carried out using the DreamTaq Green MasterMix (Thermo Fisher Scientific) or the EmeraldAmp GT PCR Master Mix (Takara Bio). Primers were obtained from Merck or Eurofins Genomics. PCR products were purified using the NucleoSpin Gel and PCR Clean-up kit (Macherey-Nagel). Restriction enzymes were of the FastDigest family of products (Thermo Fisher Scientific). Digestion products were isolated on agarose gels and purified with the NucleoSpin Gel and PCR Clean-up kit (Macherey-Nagel). Plasmid isolation was performed with NucleoSpin Plasmid kit (Macherey-Nagel). Sequence in silico manipulation was carried out using SnapGene (GSL Biotech, www.snapgene.com) and Geneious (Dotmatics). Primers were designed with NEBuilder (New England Biolabs, nebuilder.neb.com). Construct Sanger sequencing was performed by Eurofins (eurofinsgenomics.eu).

Construction of expression vectors

For full length VpOmpM1 expression in *E. coli* we inserted the VpOmpM1 CDS without the signal peptide into the pB22 vector (adding *E. coli* TamB signal peptide and seven histidine residues to the N-terminus). Briefly, we amplified the VpOmpM1 fragment with the JW203/JW202 primer pair using *V. parvula* SKV38 gDNA as a template and cloned it into pB22 digested with XhoI/XbaI, yielding the pJW46 vector. Similarly, the β-barrel portion of VpOmpM1 (pJW45) and FNLLGLLA_00518 (pB22-00518_21-200**)**, and full-length FNLLGLLA_00833 (pB22-00833) were cloned into pB22. The *ompM1* region coding for the stalk (residues 22-107) was amplified from *V. parvula* SKV38 gDNA with the primer pair stalk_F/R, digested with NcoI and XhoI, and cloned into pET28b yielding a C-terminal His_6 fusion. For the expression of full length VpOmpM1 in *V. parvula,* we inserted the C-terminal His-tagged *ompM1* coding gene containing

538 the native ribosome binding site into pRPF185 using the JW172/JW206 primer pair
539 and *V. parvula* SKV38 gDNA as a template, yielding vector pJW48. The vector was
540 then transferred by conjugation into the Δ*ompM1-3 V. parvula* mutant strain as
541 described previously[16].
542
543 **Protein expression and purification in *E. coli***
544 *E. coli* C43(DE3) Δ*cyoABCD* (Cyo complex deletion to improve purity) cells were
545 transformed with a pB22 plasmid carrying either the full-length VpOmpM1 (pJW46),
546 barrel-only VpOmpM1 (pJW45), barrel-only FNLLGLLA_00518 (pB22-00518_21-200)
547 or full-length FNLLGLLA_00833 (pB22-00833). After overnight incubation at 37°C,
548 transformants were picked from Lysogeny Broth (LB)-ampicillin plates and used to
549 inoculate a starter LB-ampicillin culture incubated at 37°C with shaking for 2 h. Flasks
550 with 1 l LB were inoculated with 8-12 ml of the starter culture and incubated at 37°C,
551 160 rpm until OD600~0.5-0.6. Protein expression was induced by supplementing the
552 cultures with 0.1% arabinose, followed by a further 3-4 h incubation at 37°C with
553 shaking. Cultures were harvested and cell pellets were stored at -20°C. Cell pellets
554 were thawed, resuspended in cold 20 mM Tris-HCl pH 8.0, 300 mM NaCl (TBS) and
555 supplemented with DNase I. Cells were lysed by passing the cell suspension once
556 through a cell disruptor (Constant Systems) at 23 kpsi. The lysate was clarified by
557 centrifugation at 30,000 x g, 4°C for 30 min. The membranes were isolated from the
558 clarified lysate by ultracentrifugation at 140,000 x g, 4°C for 50 min. The membranes
559 were solubilised in 2.5% Elugent (Millipore) in TBS for 1 h at 4°C. Insoluble material
560 was pelleted by centrifugation at 44,000 x g, 4°C for 30 min. The solubilised fraction
561 was passed through a ~4 ml chelating sepharose column charged with Ni^{2+} ions. The
562 column was washed with 20 column volumes of TBS with 30 mM imidazole and 0.15%

lauryldimethylamine oxide (LDAO), and bound protein was eluted with TBS supplemented with 200 mM imidazole and 0.2% decyl maltoside (DM). The eluate was concentrated using an Amicon Ultra filtration device (50 kDa cut-off membrane), loaded on a HiLoad Superdex 200 16/60 column and eluted in 10 mM HEPES-NaOH pH 7.5, 100 mM NaCl, 0.12% DM. Fractions were analysed by SDS-PAGE, pooled, concentrated by filtration (100 kDa cut-off membrane) and flash-frozen in liquid nitrogen. Protein samples were stored at -80°C.

E. coli BL21 (DE3) cells were transformed with the pET28b-SLH_22-107 plasmid for production of the VpOmpM1 stalk region. Expression cultures were set up as above, except kanamycin instead of ampicillin was used in all media, and protein expression was induced by adding 0.4 mM isopropyl β-D-1-thiogalactopyranoside. Protein purification was performed as above, omitting the ultracentrifugation and solubilisation steps, and without detergents in buffers. A 10 kDa cut-off membrane was used for concentrating protein.

E. coli BL21 (DE3) cells were transformed with the pBAD24-EcOmpF plasmid for production of EcOmpF. Protein expression and purification was performed as for the pB22 constructs up to the membrane isolation stage. Given that pBAD24-EcOmpF doesn't encode a His-tag, inner membranes were selectively solubilised in 20 mM HEPES-NaOH pH 7.5 and 0.5 % (w/v) sodium lauroyl sarcosinate for 30 min at room temperature with stirring. The insoluble fraction containing the outer membranes was recovered by ultracentrifugation for 30 min at 140,000 x g. The sarcosinate wash and ultracentrifugation steps were repeated once. Outer membranes were solubilised in 20 mM HEPES-NaOH pH 7.5, 50 mM NaCl and 1.5% LDAO for 1 h at 4°C. The extract was clarified by ultracentrifugation and loaded on a 1 ml ResourceQ anion exchange

column (Cytiva). The column was washed and eluted with a 0-500 mM NaCl gradient. Fractions containing EcOmpF were concentrated and subjected to size exclusion chromatography on a Superdex200 10/300 GL column (10 mM HEPES-NaOH pH 7.5, 100 mM NaCl, 0.05% LDAO). The protein was further purified on a MonoQ 5/50 GL anion exchange column (Cytiva), and detergent was exchanged to 0.12% DM via a final size exclusion chromatography run.

Expression and purification of VpOmpM1 from *V. parvula*

15 l of *V. parvula* was grown overnight in anaerobic SK media containing 1.2% sodium lactate and supplemented with 700 µg/l sodium resazurin as an oxygen indicator. Briefly, media was mixed from sterile components, boiled to remove oxygen from the solution (until resazurin appeared colourless) and flushed for 15 minutes with N_2 to remove oxygen from the bottle head volume, before being sealed with a pierceable lid. Anaerobic bottles were inoculated from overnight starter cultures at an OD of 0.04 and supplemented with 25 mg/l chloramphenicol and 250 µg/l anhydrotetracycline. Cultures were grown at 37°C overnight with 180 rpm agitation. Cells were harvested by centrifugation at 8,000 x g for 10 minutes. Pellets were pooled to represent 1.5 l of original culture each and resuspended in 5 ml HEPES pH 7.4. 100 µl $3.5x10^4$ U/ml benzonase and a small spatula of lysozyme was added and sample was incubated on ice for 15 minutes. Cells were lysed by two rounds of French press and the debris was pelleted by centrifugation for 90 minutes at 15,000 x g at 4°C. The supernatant was carefully transferred to an ultracentrifuge tube containing 2 ml of a 50% sucrose cushion and centrifuged for 4 hours at 35,000 x g. The volume at the sucrose supernatant interface was extracted, resuspended in 20 ml of HEPES pH 7.4 and

pelleted at 35,000 x g for 4 hours. Pelleted membranes were frozen in liquid nitrogen and stored at -80ºC.

V. parvula membrane solubilization and the protein purification procedure was the same as for VpOmpM1 expressed in *E. coli*, except that the flow-through from the chelating sepharose column was put through the column again due to poor binding of protein of interest to the resin. The final size exclusion chromatography step was done on a Superdex 200 10/300 Increase column.

Cryo-EM structure determination

Purified VpOmpM1 from *E. coli* (11.6 mg/ml) or *V. parvula* (8 mg/ml) was applied to glow discharged Quantifoil R 1.2/1.3 copper 200 mesh holey carbon grids. The grids were immediately blotted and plunge-frozen in liquid ethane using a Vitrobot Mark IV (ThermoFisher Scientific) device operating at 4˚C and 100% humidity. Data were collected on a FEI Glacios microscope operating at 200 kV using a Falcon 4 direct electron detector (ThermoFisher Scientific) at the University of York (Supplementary Table 1). A total of 4,284 and 6,505 movies with the *E. coli* and *V. parvula* samples, respectively, were recorded in electron event representation (EER) mode at 240,000 magnification, corresponding to a pixel size of 0.574 Å.

All image processing was done in cryoSPARC v3.3.2[79,80]. Data processing workflows are depicted in Supplementary Fig. 2. Movies were motion corrected using patch motion correction, and CTF parameters were estimated using patch CTF estimation. For VpOmpM1 expressed in *E. coli,* 2D classes generated from manually picked particles were used for template-based picking. 838,051 particles were extracted in

600 pixel boxes and Fourier cropped to 300 pixel boxes corresponding to a pixel size of 1.148 Å. Three rounds of 2D classification were used to discard bad particles, followed by generation of an ab initio 3D map using a stochastic gradient descent algorithm with 3 classes and 145,518 particles. All three classes were very similar, and a single class was used as a template in non-uniform refinement with the whole particle stack either without symmetry (C1) or with C3 symmetry enforced, with per-particle defocus and CTF group parameter (beam tilt and trefoil) refinement enabled. The 145,518 particle stack was subjected to heterogeneous refinements against the C1 map from non-uniform refinement and three decoy templates, or against the C3 map and the same three decoy templates. Particles were re-extracted in 600 pixel boxes with a pixel size of 0.574 Å. The final particle stacks (96,280 particles for the C1 map; 119,001 particles for the C3 map) were subjected to non-uniform refinement either with C1 or C3 symmetry enforced. The native VpOmpM1 dataset was processed similarly, except that two rounds of 2D classification were performed, four classes were used to make the ab initio map, four decoy templates were used in heterogeneous refinement, and the pixel size remained 1.148 Å throughout. Local resolution estimates, gold-standard Fourier shell correlations, and particle angular distribution plots for all maps are shown in Supplementary Fig. 3.

The final B-factor-sharpened maps from non-uniform refinement were used to build the models. A de novo model was built into the C3 map using Buccaneer[81] (part of CCPEM package[82]), followed by cycles of manual building in COOT[83] and real space refinement in Phenix[84]. The C3 model was then docked into the C1 map, manually extended in COOT and real-space-refined. The model built into the C1 map of VpOmpM1 expressed in *E. coli* was docked into the native VpOmpM1 C1 map,

662 manually adjusted in COOT and real-space-refined. Models were validated using
663 MolProbity[85]. Model refinement statistics are shown in Supplementary Table 1, and
664 representative map-to-model fits are shown in Supplementary Fig. 4.
665
666 **Crystal structure determination**
667 The purified VpOmpM1 stalk construct was concentrated to ~20 mg/ml. Sitting drop
668 vapour diffusion crystallisation screens were set up using a Mosquito robot (SPT
669 Labtech). Crystals grew in 0.1 M citric acid pH 3.5, 2.0 M ammonium sulphate at 20˚C.
670 Crystals were cryo-protected in mother liquor supplemented with ~20% PEG400 and
671 flash-cooled in liquid nitrogen. Diffraction data were collected at the synchrotron
672 beamline I03 at Diamond Light Source (UK) at a temperature of 100 K (Supplementary
673 Table 2). The dataset was processed with XIA2[86], scaled with Aimless[87], and the
674 space group was confirmed with Pointless[88]. Data quality was evaluated in Xtriage[84].
675 Arcimboldo[89], part of the CCP4i2 suite[90], was used for ab initio phasing. The initial
676 model was extended by Buccaneer and subjected to cycles of manual building and
677 refinement in Phenix[84] (Supplementary Table 2).
678
679 **Isolation of sacculi**
680 Peptidoglycan was isolated using the protocol of Wheeler et al.[91]. Briefly, cells were
681 grown to exponential phase, harvested and boiled for one hour in 4% SDS with
682 agitation. The resulting insoluble sacculi were isolated by ultracentrifugation at
683 150,000 x g for 2 h. The pellet was then washed by 8 rounds of resuspension in milliQ
684 H_2O and ultracentrifugation. Proteins were removed from the sample by incubating the
685 cell pellet with 100 μg/ml trypsin in digestion buffer (50 mM Tris-HCl pH 7.0, 10 mM
686 $CaCl_2$) overnight at 37°C with agitation. To inactivate and remove the trypsin, sacculi

were again boiled in 4% SDS and washed to remove residual SDS. Sacculi were then resuspended in MiliQ H_2O and lyophilized in preweighed Eppendorf tubes.

Peptidoglycan binding assay

Dry *V. parvula* and *E. coli* sacculi were resuspended in binding assay buffer (10 mM HEPES-NaOH pH 7.5, 150 mM NaCl) at 20 mg/ml. Sacculi suspensions were sonicated for 10 min in an ultrasonic bath. Binding assays with full-length and barrel-only VpOmpM1 were carried out in 200 μl aliquots, each containing binding assay buffer with 1 mg/ml sacculus suspension, ~12 μg protein, and 0.12% DM. Binding reactions were incubated at 20ºC for 2 h. The sacculi were pelleted by centrifugation in a benchtop microfuge (21,000 x g) for 15 min at 8ºC. The supernatant was saved (the soluble fraction), the pellet was resuspended in binding buffer, and the sacculi were pelleted again. The second supernatant (the wash fraction) was saved, and the pellet was resuspended in binding buffer (the pellet fraction). Samples of the soluble, wash and pellet fractions were boiled in SDS loading buffer and analysed by SDS-PAGE on 12% FastCast gels (BioRad). The SLH domain binding assay was carried out with the following modifications. 36 μg of protein was used and the detergent was omitted. The resuspended pellet fraction was split into two 100 μl aliquots, and one aliquot was supplemented with 25 U mutanolysin (Sigma) and incubated at 37ºC for 30 min. The mutanolysin digestion was included to ensure that no SLH domain that could be bound to PG was prevented from entering the gel due to insolubility of the sacculi. The SLH binding assay was analysed by SDS-PAGE using pre-cast Bis-Tris 4-12% gels (Invitrogen) in MES running buffer.

Computational Modelling & Simulation

712 **VpOmpM1 model building.** Computational models of trimeric full-length VpOmpM1
713 were predicted using AlphaFold2[45]. Two unique structures were predicted: one with
714 an extended coiled-coil stalk, and one with a compacted stalk region (Supplementary
715 Fig. 6). The AlphaFold2 predicted structure with the extended stalk displays no tilt of
716 the stalk relative to the z-axis, in contrast to the reconstructed cryo-EM density. To
717 generate a full-length VpOmpM1 structure with a tilted stalk consistent with the
718 experimental data, the extended stalk of the AlphaFold2 prediction was fit into the low
719 resolution cryo-EM density and grafted to the well-resolved experimental structure
720 using ChimeraX[92].
721
722 **System generation.** Three different models of VpOmpM1 were used to build protein-
723 membrane systems: full-length VpOmpM1 with the grafted extended stalk; full-length
724 VpOmpM1 with the compact stalk (AlphaFold2 predicted structure); and truncated
725 VpOmpM1 from the reconstructed cryo-EM density (from residue L100 onwards). For
726 each protein model, the β-barrel domain of the VpOmpM1 trimer was embedded in a
727 model *Escherichia coli* outer membrane using the CHARMM-GUI Membrane Builder
728 module[93]. The inner leaflet consisted of 90% 1-palmitoyl-2-oleoyl-sn-glycero-3-
729 phosphoethanolamine (POPE), 5% 1-palmitoyl-2-oleoyl-sn-glycero-3-
730 phosphoglycerol (POPG), and 5% 1',3'-bis[1-palmitoyl-2-oleoyl-sn-glycero-3-
731 phospho]glycerol (cardiolipin), and the outer leaflet consisted of 100% LPS (R1 core,
732 5 x O1 O-antigen units). This asymmetric bilayer system was solvated in 150 mM KCl,
733 with additional calcium ions to neutralise the LPS headgroups (~115 mM in each
734 system). The system composition is detailed in Supplementary Table 7.
735

Atomistic Molecular Dynamics Simulations. All simulations used the CHARMM36m forcefield[94] with the TIP3P water model[95]. Simulations were carried out using the GROMACS simulation package (version 2021.2)[96]. For all simulation steps, a cut-off of 1.2 nm was applied to Lennard-Jones interactions and short-range electrostatics using the potential shift Verlet scheme. Long-range electrostatics were treated using the particle mesh-Ewald (PME) method[97]. Atoms were constrained using the LINCS algorithm to allow the use of a 2 fs timestep in NPT equilibration and production phases[98]. The three systems were energy minimised in 5000 steps using the steepest descent method[99]. The subsequent systems were equilibrated in six phases (two NVT and four NPT phases) in which the protein and lipid headgroups were subjected to position restraints with varying force constants (Supplementary Table 6). All equilibration phases used the Berendsen thermostat[100] to bring the system to 303.15 K (coupling constant of 1.0 ps). NPT equilibration phases used semi-isotropic Berendsen pressure coupling scheme[100] to equilibrate with a pressure bath of 1 bar (τp = 5.0 ps, compressibility of 4.5×10^{-5} bar^{-1}).

These equilibrated systems were then simulated. The extended stalk system was simulated in duplicate for 1 μs, and the compacted and truncated stalk systems were each simulated as a single replicate for 1 μs. These production simulations utilised the Nosé-Hoover thermostat[101] (coupling constant of 1.0 ps) and the semi-isotropic Parrinello-Rahman barostat[102] (τp = 5.0 ps, compressibility of 4.5×10^{-5} bar^{-1}). Trajectories were analysed using GROMACS tools and MDAnalysis utilities[103,104]. Water orientation was analysed using a locally-written python script (available with deposited data on Zenodo). Molecular graphics and supplementary animations were generated using VMD (version 1.9.4a51)[105] and Molywood (version 0.22)[106].

OmpF Simulation. To compare the dynamics of the constriction regions, EcOmpF was also simulated. The crystal structure of trimeric EcOmpF (PDB ID: 2OMF[42]) was embedded in a model *E. coli* outer membrane and solvated using CHARMM-GUI, then equilibrated as described for the VpOmpM1 systems above. The system composition is shown in Supplementary Table 8. This system was simulated once for 500 ns under the same conditions as the above VpOmpM1 simulations.

Bilayer electrophysiology

Electrophysiology measurements were carried out in a custom-made cuvette at the centre of which was suspended a 25 μm thick Teflon film (Goodfellow Cambridge Ltd) with a 80-100 μm aperture and 1.25 ml electrode chambers either side of the film. The Teflon film aperture was made lipophilic by painting with 1.5-3 μl 1% hexadecane in hexane solution on both sides, and the hexane was allowed to evaporate for at least 30 min. Electrophysiology buffer (10 mM HEPES-KOH pH 7.5, 1 M KCl) was added to both cuvette chambers, and 3 μl of 5 mg/ml 1,2-diphytanoyl-sn-glycero-3-phosphocholine (DPhPC) dissolved in *n*-pentane was added. The *n*-pentane was allowed to evaporate for at least 5 min. DPhPC bilayers were formed using the method of Montal and Mueller[107]. Pure, concentrated protein (7-15 mg/ml) was serially diluted in 1% Genapol X-100 (Sigma). 0.3-0.5 μl of diluted protein was added to the *cis* (ground side) chamber, and diluted with electrophysiology buffer as required to promote protein insertion into the bilayer. Protein insertion events were detected as sudden jumps in current in constant-voltage mode. All measurements were carried out using Ag/AgCl pellet electrodes attached to an Axopatch 200B amplifier headstage, and a Digidata 1440A digitiser. The cuvette and headstage were enclosed in a custom-

made Faraday shield during recording. Clampex software was used for recording. Clampfit software was used to analyse data.

Liposome swelling assays

Liposome swelling assays were carried out using the method of Nikaido and Rosenberg[108] with modifications. Lipid solution (4 mg/ml phosphatidylcholine and 0.46 mg/ml dihexadecyl phosphate in chloroform) was dried under an air stream, and completely dried under vacuum for at least 2 h. 80 μl of lipid solution was used per condition, *i.e.* per protein to be reconstituted. The dried lipids were resuspended in 100 μl deionised water per condition. Equimolar amounts of protein were added to the resuspended lipid so that the total protein quantity was 15-30 μg, followed by immediate vortexing. All conditions were supplemented with DM containing buffer to ensure that equal amounts of detergent were present in all samples. DM-containing buffer was added to control liposomes. Solutions were sonicated in a water bath for 1-1.5 min until translucent, and dried under vacuum overnight. The following day the proteoliposomes were rehydrated in 200 μl 10 mM HEPES-NaOH pH 7.5 and 12 mM stachyose per condition for 1-2 h at room temperature. Control liposomes were used to determine the concentration of each substrate that is isosmotic to the intraliposomal milieu (i.e. there is no swelling of the control liposomes), usually between 7.5 and 15 mM substrate in 10 mM HEPES-NaOH pH 7.5. Substrate concentrations used can be found in Supplementary Table 9. The decrease in A_{400} due to liposome swelling was measured after adding 200 μl of the substrate solution to 15 μl of the proteoliposome suspension. Readings were taken on a Perkin Elmer Lambda 35 spectrophotometer in 1 s intervals for 30 s. A line was fit to the absorbance data corresponding to the linear phase of swelling (2-15 s), and the slope of the line was recorded as the swelling

811 rate. Control liposome swelling rates were subtracted from all proteoliposome swelling
812 rates. All data were normalized to EcOmpF-containing liposome swelling in the
813 presence of arabinose.
814
815

Data availability

Electron microscopy maps have been deposited in the Electron Microscopy Data Bank with the accession codes EMD-16328 [https://www.ebi.ac.uk/pdbe/entry/emdb/EMD-16328] (VpOmpM1 from *E. coli* in C1), EMD-16333 [https://www.ebi.ac.uk/pdbe/entry/emdb/EMD-16333] (VpOmpM1 from *E. coli* in C3) and EMD-16332 [https://www.ebi.ac.uk/pdbe/entry/emdb/EMD-16332] (VpOmpM1 from *V. parvula* in C1). Atomic coordinates have been deposited in the Protein Data Bank under accession codes 8BYM [https://doi.org/10.2210/pdb8BYM/pdb] (VpOmpM1 from *E. coli* in C1), 8BYT [https://doi.org/10.2210/pdb8BYT/pdb] (VpOmpM1 from *E. coli* in C3), 8BYS [https://doi.org/10.2210/pdb8BYS/pdb] (VpOmpM1 from *V. parvula* in C1), and 8BZ2 [https://doi.org/10.2210/pdb8BZ2/pdb] (VpOmpM1 stalk crystal structure). The following atomic coordinates used for comparison purposes were downloaded from the Protein Data Bank: 3PYW [https://doi.org/10.2210/pdb3PYW/pdb], 6CWH [https://doi.org/10.2210/pdb6CWH/pdb], 3POQ [https://doi.org/10.2210/pdb3POQ/pdb], 5F7L [https://doi.org/10.2210/pdb5F7L/pdb], 2OMF [https://doi.org/10.2210/pdb2OMF/pdb], 2ZFG [https://doi.org/10.2210/pdb2ZFG/pdb], 8AGD [https://doi.org/10.2210/pdb8AGDpdb]. Trajectories and run input files for the Molecular Dynamics simulations are available on Zenodo (https://doi.org/10.5281/zenodo.8239075). Source data for electrophysiology, liposome swelling assays, and HOLE and MD analyses are available. Other data presented in this paper, constructs and strains are available on reasonable request.

Code availability

The water orientation analysis script is available on Zenodo (https://doi.org/10.5281/zenodo.8239075).

References

1. Silhavy, T. J., Ruiz, N. & Kahne, D. Advances in understanding bacterial outer-membrane biogenesis. *Nat. Rev. Microbiol*. 2006 41 4, 57–66 (2006).

2. Sun, J., Rutherford, S. T., Silhavy, T. J. & Huang, K. C. Physical properties of the bacterial outer membrane. *Nat. Rev. Microbiol.* 20, 236–248 (2022).

3. Bladen, H. A. & Mergenhagen, S. E. Ultrastructure of *Veillonella* and morphological correlation of an outer membrane with particles associated with endotoxic activity. *J. Bacteriol*. 88, 1482 (1964).

4. Rojas, E. R. et al. The outer membrane is an essential load-bearing element in Gram-negative bacteria. *Nature* 559, 617–621 (2018).

5. Braun, V. & Rehn, K. Chemical Characterization, Spatial Distribution and Function of a Lipoprotein (Murein-Lipoprotein) of the *E. coli* Cell Wall. *Eur. J. Biochem*. 10, 426–438 (1969).

6. Braun, V. Covalent lipoprotein from the outer membrane of *Escherichia coli*. *Biochim. Biophys. Acta - Rev. Biomembr.* 415, 335–377 (1975).

7. Cascales, E., Bernadac, A., Gavioli, M., Lazzaroni, J. C. & Lloubes, R. Pal lipoprotein of *Escherichia coli* plays a major role in outer membrane integrity. *J. Bacteriol.* 184, 754–759 (2002).

8. Bouveret, E., Bénédetti, H., Rigal, A., Loret, E. & Lazdunski, C. In vitro characterization of peptidoglycan-associated lipoprotein (PAL)- peptidoglycan and PAL-TolB interactions. *J. Bacteriol.* 181, 6306–6311 (1999).

9. Parsons, L. M., Lin, F. & Orban, J. Peptidoglycan recognition by Pal, an outer membrane lipoprotein. *Biochemistry* 45, 2122–2128 (2006).

10. Park, J. S. et al. Mechanism of anchoring of OmpA protein to the cell wall peptidoglycan of the gram-negative bacterial outer membrane. *FASEB J.* 26, 219–228 (2012).

11. Samsudin, F., Boags, A., Piggot, T. J. & Khalid, S. Braun's Lipoprotein Facilitates OmpA Interaction with the *Escherichia coli* Cell Wall. *Biophys. J.* 113, 1496–1504 (2017).

12. Sonntag, I., Schwarz, H., Hirota, Y. & Henning, U. Cell envelope and shape of *Escherichia coli*: multiple mutants missing the outer membrane lipoprotein and other major outer membrane proteins. *J. Bacteriol*. 136, 280 (1978).

13. Suzuki, H. et al. Murein-lipoprotein of *Escherichia coli:* a protein involved in the stabilization of bacterial cell envelope. *Mol. Gen. Genet.* 167, 1–9 (1978).

14. Bernadac, A., Gavioli, M., Lazzaroni, J. C., Raina, S. & Lloubès, R. *Escherichia coli tol-pal* mutants form outer membrane vesicles*. J. Bacteriol*. 180, 4872–4878 (1998).

15. Wang, Y. The Function of OmpA in *Escherichia coli*. *Biochem. Biophys. Res. Commun.* 292, 396–401 (2002).

16. Witwinowski, J. et al. An ancient divide in outer membrane tethering systems in bacteria suggests a mechanism for the diderm-to-monoderm transition. *Nat. Microbiol.* 7, 411–422 (2022).

17. Kalmokoff, M. L. et al. Physical and genetic characterization of an outer-membrane protein (OmpM1) containing an N-terminal S-layer-like homology domain from the phylogenetically Gram-positive gut anaerobe *Mitsuokella multacida*. *Anaerobe* 15, 74–81 (2009).

18. Kojima, S. et al. Cadaverine covalently linked to peptidoglycan is required for interaction between the peptidoglycan and the periplasm-exposed S-layer-

893 homologous domain of major outer membrane protein Mep45 in *Selenomonas*
894 *ruminantium. J. Bacteriol.* 192, 5953–5961 (2010).
895 19. Kojima, S. et al. Peptidoglycan-associated outer membrane protein Mep45 of
896 rumen anaerobe *Selenomonas ruminantium* forms a non-specific diffusion pore via its
897 C-terminal transmembrane domain. *Biosci. Biotechnol. Biochem*. 80, 1954 (2016).
898 20. Kowata, H., Tochigi, S., Takahashi, H. & Kojima, S. Outer Membrane
899 Permeability of Cyanobacterium *Synechocystis* sp. Strain PCC 6803: Studies of
900 Passive Diffusion of Small Organic Nutrients Reveal the Absence of Classical Porins
901 and Intrinsically Low Permeability*. J. Bacteriol*. 199, (2017).
902 21. Ravi, J. & Fioravanti, A. S-layers: The Proteinaceous Multifunctional Armors of
903 Gram-Positive Pathogens. *Front. Microbiol*. 12, 663468 (2021).
904 22. Mesnage, S. et al. Bacterial SLH domain proteins are non-covalently anchored
905 to the cell surface via a conserved mechanism involving wall polysaccharide
906 pyruvylation. *EMBO J.* 19, 4473–4484 (2000).
907 23. Kern, J., Ryan, C., Faull, K. & Schneewind, O. *Bacillus anthracis* Surface-Layer
908 Proteins Assemble by Binding to the Secondary Cell Wall Polysaccharide in a Manner
909 that Requires *csaB* and *tagO*. *J. Mol. Biol.* 401, 757–775 (2010).
910 24. Missiakas, D. & Schneewind, O. Assembly and Function of the *Bacillus*
911 *anthracis S-Layer*. *Annu. Rev. Microbiol.* 71, 79–98 (2017).
912 25. Olabarría, C., Carrascosa, J. L., De Pedro, M. A. & Berenguer, J. A conserved
913 motif in S-layer proteins is involved in peptidoglycan binding in *Thermus thermophilus*.
914 *J. Bacteriol*. 178, 4765 (1996).
915 26. Cava, F., De Pedro, M. A., Schwarz, H., Henne, A. & Berenguer, J. Binding to
916 pyruvylated compounds as an ancestral mechanism to anchor the outer envelope in
917 primitive bacteria. *Mol. Microbiol*. 52, 677–690 (2004).

27. Kojima, S. & Okumura, Y. Outer membrane-deprived cyanobacteria liberate periplasmic and thylakoid luminal components that support the growth of heterotrophs. *bioRxiv* 2020.03.24.006684 (2020). doi:10.1101/2020.03.24.006684

28. Kamio, Y., Itoh, Y. & Terawaki, Y. Chemical structure of peptidoglycan in *Selenomonas ruminantium*: Cadaverine links covalently to the D-glutamic acid residue of peptidoglycan*. J. Bacteriol.* 146, 49–53 (1981).

29. Kamio, Y. & Nakamura, K. Putrescine and cadaverine are constituents of peptidoglycan in *Veillonella alcalescens* and *Veillonella parvula. J. Bacteriol.* 169, 2881–2884 (1987).

30. Fernandez-Herrero, L. A., Olabarria, G., Caston, J. R., Lasa, I. & Berenguer, J. Horizontal transference of S-layer genes within *Thermus thermophilus. J. Bacteriol*. 177, 5460 (1995).

31. Rothfuss, H., Lara, J. C., Schmid, A. K. & Lidstrom, M. E. Involvement of the S-layer proteins Hpi and SlpA in the maintenance of cell envelope integrity in *Deinococcus radiodurans* R1. *Microbiology* 152, 2779–2787 (2006).

32. von Kügelgen, A., van Dorst, S., Alva, V. & Bharat, T. A. M. A multidomain connector links the outer membrane and cell wall in phylogenetically deep-branching bacteria. *Proc. Natl. Acad. Sci. U. S. A.* 119, e2203156119 (2022).

33. Nikaido, H. & Vaara, M. Molecular basis of bacterial outer membrane permeability. *Microbiol. Rev.* 49, 1 (1985).

34. Nikaido, H. Molecular basis of bacterial outer membrane permeability revisited. *Microbiol. Mol. Biol. Rev*. 67, 593–656 (2003).

35. Ruggiu, F. et al. Size Matters and How You Measure It: A Gram-Negative Antibacterial Example Exceeding Typical Molecular Weight Limits. *ACS Infect. Dis*. 5, 1688–1692 (2019).

943 36. Poppleton, D. I. et al. Outer Membrane Proteome of *Veillonella parvula*: A
944 Diderm Firmicute of the Human Microbiome. *Front. Microbiol*. 8, (2017).
945 37. Farci, D. et al. The cryo-EM structure of the S-layer deinoxanthin-binding
946 complex of *Deinococcus radiodurans* informs properties of its environmental
947 interactions. *J. Biol. Chem*. 298, (2022).
948 38. Farci, D., Graça, A. T., Iesu, L., de Sanctis, D. & Piano, D. The SDBC is active
949 in quenching oxidative conditions and bridges the cell envelope layers in *Deinococcus*
950 *radiodurans. J. Biol. Chem*. 299, 102784 (2023).
951 39. Farci, D., Haniewicz, P. & Piano, D. The structured organization of *Deinococcus*
952 *radiodurans*' cell envelope. *Proc. Natl. Acad. Sci. U. S. A*. 119, e2209111119 (2022).
953 40. von Kügelgen, A. et al. Interdigitated immunoglobulin arrays form the
954 hyperstable surface layer of the extremophilic bacterium *Deinococcus radiodurans*.
955 *Proc. Natl. Acad. Sci. U. S. A.* 120, e2215808120 (2023).
956 41. Cowan, S. W. et al. Crystal structures explain functional properties of two *E.*
957 *coli* porins. *Nature* 358, 727–733 (1992).
958 42. Baslé, A., Rummel, G., Storici, P., Rosenbusch, J. P. & Schirmer, T. Crystal
959 structure of osmoporin OmpC from *E. coli* at 2.0 A. *J. Mol. Biol*. 362, 933–942 (2006).
960 43. Xie, Y. et al. IBS 2.0: an upgraded illustrator for the visualization of biological
961 sequences. *Nucleic Acids Res*. 50, W420–W426 (2022).
962 44. Jumper, J. et al. Highly accurate protein structure prediction with AlphaFold.
963 *Nature* 2021 596, 583–589 (2021).
964 45. Kern, J. et al. Structure of Surface Layer Homology (SLH) Domains from
965 *Bacillus anthracis* Surface Array Protein. *J. Biol. Chem*. 286, 26042–26049 (2011).
966 46. Blackler, R. J. et al. Structural basis of cell wall anchoring by SLH domains in
967 *Paenibacillus alvei. Nat. Commun.* 2018 91 9, 1–11 (2018).

968 47. Sychantha, D. et al. Molecular Basis for the Attachment of S-Layer Proteins to
969 the Cell Wall of *Bacillus anthracis*. *Biochemistry* 57, 1949–1953 (2018).
970 48. Legg, M. S. G. et al. The S-layer homology domains of *Paenibacillus alvei*
971 surface protein SpaA bind to cell wall polysaccharide through the terminal
972 monosaccharide residue. *J. Biol. Chem*. 298, 101745 (2022).
973 49. Vassylyev, D. G., Tomitori, H., Kashiwagi, K., Morikawa, K. & Igarashi, K.
974 Crystal Structure and Mutational Analysis of the *Escherichia coli* Putrescine Receptor:
975 STRUCTURAL BASIS FOR SUBSTRATE SPECIFICITY. *J. Biol. Chem*. 273, 17604–
976 17609 (1998).
977 50. Wu, D. et al. Structural Basis of Substrate Binding Specificity Revealed by the
978 Crystal Structures of Polyamine Receptors SpuD and SpuE from *Pseudomonas*
979 *aeruginosa. J. Mol. Biol*. 416, 697–712 (2012).
980 51. Bale, S. et al. Structural basis for putrescine activation of human S-
981 adenosylmethionine decarboxylase. *Biochemistry* 47, 13404–13417 (2008).
982 52. Sagong, H. Y. et al. Crystal Structure and Pyridoxal 5-Phosphate Binding
983 Property of Lysine Decarboxylase from *Selenomonas ruminantium. PLoS One* 11,
984 e0166667 (2016).
985 53. Kröger, P., Shanmugaratnam, S., Ferruz, N., Schweimer, K. & Höcker, B. A
986 comprehensive binding study illustrates ligand recognition in the periplasmic binding
987 protein PotF. *Structure* 29, 433-443.e4 (2021).
988 54. Ashkenazy, H. et al. ConSurf 2016: an improved methodology to estimate and
989 visualize evolutionary conservation in macromolecules. *Nucleic Acids Res*. 44, W344–
990 W350 (2016).
991 55. Holm, L. Dali server: structural unification of protein families. *Nucleic Acids Res*.
992 50, W210–W215 (2022).

56. Moonens, K. et al. Structural Insights into Polymorphic ABO Glycan Binding by *Helicobacter pylori. Cell Host Microbe* 19, 55–66 (2016).

57. Smart, O. S., Neduvelil, J. G., Wang, X., Wallace, B. A. & Sansom, M. S. P. HOLE: A program for the analysis of the pore dimensions of ion channel structural models*. J. Mol. Graph*. 14, 354–360 (1996).

58. Vasan, A. K. et al. Role of internal loop dynamics in antibiotic permeability of outer membrane porins. *Proc. Natl. Acad. Sci. U. S. A.* 119, e2117009119 (2022).

59. Gutiérrez, S. A., Bodrenko, I., Scorciapino, M. A. & Ceccarelli, M. Macroscopic electric field inside water-filled biological nanopores. *Phys. Chem. Chem. Phys*. 18, 8855–8864 (2016).

60. Bajaj, H. et al. Bacterial Outer Membrane Porins as Electrostatic Nanosieves: Exploring Transport Rules of Small Polar Molecules. *ACS Nano* 11, 5465–5473 (2017).

61. Nestorovich, E. M., Rostovtseva, T. K. & Bezrukov, S. M. Residue Ionization and Ion Transport through OmpF Channels. *Biophys. J*. 85, 3718–3729 (2003).

62. Schmitt, E. K., Vrouenraets, M. & Steinem, C. Channel activity of OmpF monitored in nano-BLMs. *Biophys. J*. 91, 2163–2171 (2006).

63. Efremov, R. G. & Sazanov, L. A. Structure of *Escherichia coli* OmpF porin from lipidic mesophase. *J. Struct. Biol.* 178, 311–318 (2012).

64. Vandeputte-Rutten, L. et al. Crystal structure of the outer membrane protease OmpT from *Escherichia coli* suggests a novel catalytic site. *EMBO J.* 20, 5033–5039 (2001).

65. Eren, E., Murphy, M., Goguen, J. & van den Berg, B. An Active Site Water Network in the Plasminogen Activator Pla from *Yersinia pestis. Structure* 18, 809–818 (2010).

66. Hong, H., Patel, D. R., Tamm, L. K. & Van Den Berg, B. The Outer Membrane Protein OmpW Forms an Eight-stranded β-Barrel with a Hydrophobic Channel. *J. Biol. Chem.* 281, 7568–7577 (2006).

67. Hong, H., Szabo, G. & Tamm, L. K. Electrostatic couplings in OmpA ion-channel gating suggest a mechanism for pore opening. *Nat. Chem. Biol.* 2006 211 2, 627–635 (2006).

68. Mader, C., Huber, C., Moll, D., Sleytr, U. B. & Sára, M. Interaction of the Crystalline Bacterial Cell Surface Layer Protein SbsB and the Secondary Cell Wall Polymer of *Geobacillus stearothermophilus* PV72 Assessed by Real-Time Surface Plasmon Resonance Biosensor Technology. *J. Bacteriol*. 186, 1758–1768 (2004).

69. Janesch, B., Messner, P. & Schäffer, C. Are the surface layer homology domains essential for cell surface display and glycosylation of the S-layer protein from *Paenibacillus alvei* CCM 2051T? *J. Bacteriol*. 195, 565–575 (2013).

70. von Kügelgen, A. et al. Interdigitated immunoglobulin arrays form the hyperstable surface layer of the extremophilic bacterium *Deinococcus radiodurans*. *bioRxiv* 2022.09.15.508085 (2022). doi:10.1101/2022.09.15.508085

71. Merino, N. et al. Living at the extremes: Extremophiles and the limits of life in a planetary context. *Front. Microbiol*. 10, 447668 (2019).

72. Green, M. R. & Sambrook, J. Molecular Cloning: A Laboratory Manual (Fourth Edition). (*Cold Spring Harbor Laboratory Press*, 2012).

73. Knapp, S. et al. Natural Competence Is Common among Clinical Isolates of *Veillonella parvula* and Is Useful for Genetic Manipulation of This Key Member of the Oral Microbiome. *Front. Cell. Infect. Microbiol*. 7, (2017).

74. Béchon, N. et al. Autotransporters Drive Biofilm Formation and Autoaggregation in the Diderm Firmicute *Veillonella parvula*. *J. Bacteriol*. 202, (2020).

1043 75. Inoue, H., Nojima, H. & Okayama, H. High efficiency transformation of
1044 *Escherichia coli* with plasmids. *Gene* 96, 23–28 (1990).
1045 76. Jacques, I. B. et al. Analysis of 51 cyclodipeptide synthases reveals the basis
1046 for substrate specificity. *Nat. Chem. Biol.* 119 11, 721–727 (2015).
1047 77. Knapp, S. et al. Natural Competence Is Common among Clinical Isolates of
1048 *Veillonella parvula* and Is Useful for Genetic Manipulation of This Key Member of the
1049 Oral Microbiome. *Front. Cell. Infect. Microbiol*. 7, 139 (2017).
1050 78. Punjani, A., Rubinstein, J. L., Fleet, D. J. & Brubaker, M. A. cryoSPARC:
1051 algorithms for rapid unsupervised cryo-EM structure determination. *Nat. Methods* 143
1052 14, 290–296 (2017).
1053 79. Punjani, A., Zhang, H. & Fleet, D. J. Non-uniform refinement: adaptive
1054 regularization improves single-particle cryo-EM reconstruction. *Nat. Methods* 1712 17,
1055 1214–1221 (2020).
1056 80. Hoh, S. W., Burnley, T. & Cowtan, K. Current approaches for automated model
1057 building into cryo-EM maps using Buccaneer with CCP-EM. *Acta Crystallogr. Sect. D,*
1058 *Struct. Biol.* 76, 531–541 (2020).
1059 81. Wood, C. et al. Collaborative Computational Project for Electron cryo-
1060 Microscopy. *Acta Crystallogr. Sect. D Biol. Crystallogr*. 71, 123–126 (2015).
1061 82. Emsley, P., Lohkamp, B., Scott, W. G. & Cowtan, K. Features and development
1062 of Coot. *Acta Crystallogr. D. Biol. Crystallogr*. 66, 486–501 (2010).
1063 83. Liebschner, D. et al. Macromolecular structure determination using X-rays,
1064 neutrons and electrons: recent developments in Phenix. *Acta Crystallogr. Sect. D*,
1065 *Struct. Biol.* 75, 861–877 (2019).
1066 84. Chen, V. B. et al. MolProbity: all-atom structure validation for macromolecular
1067 crystallography. *Acta Crystallogr. D. Biol. Crystallogr*. 66, 12–21 (2010).

85. Winter, G. Xia2: An expert system for macromolecular crystallography data reduction. *J. Appl. Crystallogr*. 43, 186–190 (2010).

86. Evans, P. R. & Murshudov, G. N. How good are my data and what is the resolution? *Acta Crystallogr. Sect. D Biol. Crystallogr*. 69, 1204–1214 (2013).

87. Evans, P. Scaling and assessment of data quality. *Acta Crystallographica Section D: Biological Crystallography* 62, 72–82 (International Union of Crystallography, 2006).

88. Rodríguez, D. D. et al. Crystallographic ab initio protein structure solution below atomic resolution. *Nat. Methods* 2009 69 6, 651–653 (2009).

89. Potterton, L. et al. CCP4i2: the new graphical user interface to the CCP4 program suite. *Acta Crystallogr. Sect. D, Struct. Biol*. 74, 68 (2018).

90. Wheeler, R., Veyrier, F., Werts, C. & Boneca, I. G. Peptidoglycan and Nod Receptor. *Glycosci. Biol. Med*. 1–10 (2014).

91. Pettersen, E. F. et al. UCSF ChimeraX: Structure visualization for researchers, educators, and developers. *Protein Sci.* 30, 70–82 (2021).

92. Lee, J. et al. CHARMM-GUI Membrane Builder for Complex Biological Membrane Simulations with Glycolipids and Lipoglycans. *J. Chem. Theory Comput.* 15, 775–786 (2019).

93. Huang, J. & Mackerell, A. D. CHARMM36 all-atom additive protein force field: Validation based on comparison to NMR data. *J. Comput. Chem.* 34, 2135–2145 (2013).

94. Jorgensen, W. L., Chandrasekhar, J., Madura, J. D., Impey, R. W. & Klein, M. L. Comparison of simple potential functions for simulating liquid water. *J. Chem. Phys*. 79, 926 (1998).

95. Van Der Spoel, D. et al. GROMACS: Fast, flexible, and free. *Journal of Computational Chemistry* 26, 1701–1718 (2005).

96. Essmann, U. et al. A smooth particle mesh Ewald method. *J. Chem. Phys*. 103, 8577–8593 (1995).

97. Hess, B., Bekker, H., Berendsen, H. J. C. & Fraaije, J. G. E. M. LINCS: A Linear Constraint Solver for molecular simulations. *J. Comput. Chem*. 18, 1463–1472 (1997).

98. Goldstein, A. A. On Steepest Descent. *J. Soc. Ind. Appl. Math. Ser. A Control* 3, 147–151 (1965).

99. Berendsen, H. J. C., Postma, J. P. M., Van Gunsteren, W. F., Dinola, A. & Haak, J. R. Molecular dynamics with coupling to an external bath. *J. Chem. Phys*. 81, 3684–3690 (1984).

100. Nosé, S. A unified formulation of the constant temperature molecular dynamics methods. *J. Chem. Phys.* 81, 511–519 (1984).

101. Parrinello, M. & Rahman, A. Polymorphic transitions in single crystals: A new molecular dynamics method. *J. Appl. Phys.* 52, 7182 (1998).

102. Michaud-Agrawal, N., Denning, E. J., Woolf, T. B. & Beckstein, O. MDAnalysis: A toolkit for the analysis of molecular dynamics simulations. *J. Comput. Chem*. 32, 2319–2327 (2011).

103. Gowers, R. et al. MDAnalysis: A Python Package for the Rapid Analysis of Molecular Dynamics Simulations. *Proceedings of the 15th Python in Science Conference* 98–105 (SciPy, 2016). doi:10.25080/Majora-629e541a-00e

104. Humphrey, W., Dalke, A. & Schulten, K. VMD: Visual molecular dynamics. *J. Mol. Graph.* 14, 33–38 (1996).

105. Wieczór, M., Hospital, A., Bayarri, G., Czub, J. & Orozco, M. Molywood: streamlining the design and rendering of molecular movies. *Bioinformatics* 36, 4660–4661 (2020).

106. Montal, M. & Mueller, P. Formation of Bimolecular Membranes from Lipid Monolayers and a Study of Their Electrical Properties. *Proc. Natl. Acad. Sci. U. S. A.* 69, 3561 (1972).

107. Nikaido, H. & Rosenberg, E. Y. Porin channels in *Escherichia coli*: studies with liposomes reconstituted from purified proteins. *J. Bacteriol.* 153, 241–252 (1983).

Acknowledgements

We thank the University of York (UK) electron cryo-microscopy facility for access to instrumentation and support. We acknowledge the Diamond Light Source for I03 beamline access (proposal mx-24948) and support. We thank David Staunton (University of Oxford) for carrying out the dynamic scanning calorimetry experiments. This work was supported by a Wellcome Trust Investigator award (214222/Z/18/Z) to B.v.d.B., providing salary support to A.S. and Y.Z. C.B., S.G., J.W., and R.E.S. were supported by funding from the French National Research Agency (ANR) (no. Fir-OM ANR-16-CE12-0010), the Institut Pasteur Programmes Transversaux de Recherche (no. PTR 39-16), and the French government Investissement d'Avenir Program, Laboratoire d'Excellence Integrative Biology of Emerging Infectious Diseases (grant no. ANR-10-LABX-62-IBEID). The authors acknowledge the use of the IRIDIS High Performance Computing Facility, and associated support services at the University of Southampton, in the completion of this work. K.E.N. was supported by a Ph.D. Studentship from the Engineering and Physical Sciences Research Council (Project Number: 2446840), and S.K. by an EPSRC established Career Fellowship (EPSRC grant no. EP/V030779/1).

Author contributions

A.S. made constructs, purified proteins, determined cryo-EM and crystal structures, carried out functional assays, and wrote the manuscript with input from all authors. Y.Z. purified proteins and carried out functional assays. J.W. made constructs and strains and prepared the dataset for ConSurf analysis. R.E.S. grew *V. parvula*, prepared membrane pellets, and isolated sacculi. K.E.N. performed simulations, supervised by S.K. S.P.B. collected preliminary electrophysiology data. A.B. collected

X-ray diffraction data and managed the Newcastle Structural Biology Laboratory. B.v.d.B. made constructs, purified and crystallised proteins. S.G., C.B. and B.v.d.B. conceived and supervised the project.

Competing Interests

The authors declare no competing interests.

Figure Legends

Figure 1. Cryo-EM structures of VpOmpM1 expressed in *E. coli* and *V. parvula*. **a** Schematic depicting VpOmpM1 (UniProt A0A100YN03) domain arrangement and boundaries. SP, signal peptide; SLH, S-layer homology; CC, coiled coil. Generated using IBS 2.0[44]. **b** Structure of recombinant VpOmpM1. The cryo-EM density is shown on the left and the model is shown on the right as viewed towards the OM from outside the cell. **c** Representative 2D class averages. White arrowheads point to the diffuse SLH domain density. The edge of each square is 344.4 Å long. **d** Side view of the cryo-EM density at high (left) and low (right) contour level. The grey bar represents the outer membrane (OM). The diffuse grey density around the membrane region in the high contour view likely corresponds to lipid or detergent. **e** Superposition of structures from recombinant VpOmpM1 (in colour) and native VpOmpM1 purified from *V. parvula* (white). **f** Superposition of coiled-coils of protomers from the recombinant (yellow, pink, blue) and native (grey, white, black) VpOmpM1 structures. The structural alignment was performed on the β-barrel region only (not shown). Left – side view, right – view from the periplasm towards the OM. **g, h** Inter-protomer contacts at the β-barrel-stalk interface in the recombinant (**g**) and native (**h**) structures. The protomer (A, B, C) for each sidechain is indicated in superscript.

Figure 2. All-atom molecular dynamics simulations with native VpOmpM1. **a** The AlphaFold2 prediction for the stalk (grey) was grafted onto the N-terminus of the first residue (L100) modelled into the experimental density of native VpOmpM1 (in colour). R64 (bottom of SLH domain) and R113 are shown as space filling models. **b** Bird's-eye-view of the β-barrel region from outside the OM (left) and a plot of the stalk end projection (centre of mass of the R64 Cα atoms) over the 1 μs simulation (right). The observation point in the left and right panels is equivalent. **c** Frequency distribution of stalk lengths (R64-R113 Cα-Cα) observed throughout the simulation. **d** Distances between the R113 sidechain and interacting sidechain atoms throughout the simulation. The dotted line denotes an inter-atomic distance of 3 Å. The equivalent plots for a replicate simulation and a simulation without the AlphaFold2 graft are presented in Supplementary Fig. 5.

Figure 3. Analysis of the putative peptidoglycan binding site within the SLH domain. a Binding assay of recombinant full-length and barrel-only VpOmpM1 to sacculi (PG) isolated from *V. parvula* and *E. coli.* After incubation of protein with PG, the insoluble PG was pelleted by centrifugation, washed by resuspending in buffer, and pelleted again. The supernatant from the binding reaction (S), the wash (W) and the resuspended PG pellet (P) were boiled and analysed by SDS-PAGE. Three independent binding experiments were performed and yielded similar results. **b** Close up view of the VparOmpM1 SLH domains predicted by AlphaFold2, the crystal structure of SLH domains 1-3 from *Bacillus anthracis* Sap (surface array protein) (PDB 3PYW)[46], and the crystal structure of SLH domains 1-3 from *Paenibacillus alvei* SpaA in complex with the monosaccharide 4,6-pyr-β-D-ManNAcOMe (space-filling representation) (PDB 6CWH)[47]. Views were generated from a superposition. **c** Multiple sequence alignment results from different subsets of SLH domain-containing proteins mapped onto the sequence of VpOmM1 SLH domain and coloured by conservation using ConSurf [55] (colour key). Row 1 - OmpM homologues from Negativicutes; row 2 – representative OmpM homologues from all diderm Firmicutes; row 3 – representative OmpM homologues from diderm Terrabacteria, excluding

Firmicutes; row 4 – SLH domains from non-OmpM from diderm Firmicutes. The arrows point to Y36 and Y65, which could be important for binding polyaminated PG. **d** ConSurf results mapped onto the predicted SLH domains of VpOmpM1 (same sequence subsets and colour key as **b**). Arrows point to the grooves between SLH protomers. Y36 is shown in space-filling representation. The datasets used for ConSurf analysis correspond to the datasets used in a previous study[16] that were subsampled using custom scripts. **e** Conserved residues shown as stick models on the predicted SLH structure, coloured by chain, except for Y36 and Y65 which are in purple. SpaA bound to monosaccharide (PDB 6CWH) was superposed onto the VpOmpM1 SLH structure; the monosaccharide is in grey, the SpaA protein model is not shown.

Figure 4. Crystallography, AlphaFold2, and binding assay show evidence of alternate stalk conformations. a Crystal structure of VpOmpM1 stalk trimer at 1.7 Å. Residues 23-105 were resolved. One chain is in rainbow: N-terminus is blue, C-terminus is red. **b** Electrostatic surface presentation of the stalk crystal structure. (Left) Putative view from the OM and (right) from the periplasm. **c** Comparison of the stalk crystal structure (left) and AlphaFold2 predicted extended conformation (middle). Only residues 23-105 are displayed for both. (Right) Residues 64-105 of the stalk crystal structure that form the extended coiled-coil in the AlphaFold2 prediction are in grey. **d** Alternative, compact stalk conformation predicted by AlphaFold2. **e** Close up view of the compact stalk prediction with a single chain from the crystal structure (black) superposed (Cα-Cα r.m.s.d. 0.78 Å) (left). (Middle) Top view down the section marked by the dashed line. (Right) Stalk crystal structure. The sidechain of M75 is shown in green space-filling representation in each panel. **f** Binding assay of recombinant VpOmpM1 SLH domain to sacculi (PG) isolated from *V. parvula* and *E. coli.* After incubation of protein with PG, the insoluble PG was pelleted by centrifugation, washed by resuspending in buffer, and pelleted again. The PG was then resuspended and split into two aliquots, one of which was incubated with mutanolysin (Mut). The supernatant from the binding reaction (S), the wash (W) and the resuspended PG pellet without (P) and with Mut treatment (P_{Mut}) were boiled and analysed by SDS-PAGE. Three independent binding experiments were performed and yielded similar results. **g** All-atom MD simulation of AlphaFold2 predicted compact stalk model over 1 μs. The SLH domain of one of the protomers (pink) reaches towards the OM and interacts with the periplasmic turns of the β-barrel of another protomer (blue). The salt bridges shown on the right had occupancies of 5.8%, 3.44% and 1.89% (top to bottom) throughout the simulation.

Figure 5. VpOmpM1 and EcOmpF eyelet comparison. **a** β-barrel from the C3 cryo-EM reconstruction of VpOmpM1 (top) and an EcOmpF protomer (PDB 3POQ)[64] (bottom). The views are generated from a superposition. VpOmpM1 loops 3 and 7 are in green and orange, respectively; EcOmpF loop 3 is in black. Residues forming the eyelet are shown in stick representation. **b** Close-up view of the eyelet regions of VpOmpM1 (top) and EcOmpF (bottom). Colours as in **a**. Positively and negatively charged residues lining the eyelet are annotated with a blue plus or red minus sign, respectively. **c** HOLE[58] profiles calculated from aligned experimental structures of VpOmpM1 β-barrel and EcOmpF. The z-coordinate is perpendicular to the membrane plane and its origin is at the narrowest part of the VpOmpM1 eyelet.

Figure 6. VpOmpM1 channel properties. a Liposome swelling in the presence of indicated substrate. Liposomes with embedded full-length VpOmpM1, VpOmpM1 barrel-only or EcOmpF were tested. Swelling rates were normalised to the rate of swelling of EcOmpF-containing liposomes in the presence of arabinose. Each condition was measured in technical triplicates (except EcOmpF with fructose, where n=2) from the same proteoliposome preparation. Error bars show mean ± SD. **b** Bilayer electrophysiology conductance distribution plots obtained from recordings with multiple insertion events (see Supplementary Fig. 15 for representative traces). Full-length VpOmpM1 distribution is centred on 4.87 ± 1.86 nS (SD, n=117); VpOmpM1 barrel-only distribution is centred on 4.66 ± 1.88 nS (SD, n=269). **c** Representative bilayer electrophysiology recordings of full-length VpOmpM1 (top) showing multiple sub-conductance states and of the barrel-only construct (bottom) showing classical trimeric porin sequential channel closure at high voltage. **d** Current-voltage characteristics from single channel recordings of full-length VpOmpM1 (n=4), barrel-only VpOmpM1 (n=4), and EcOmpF (n=3). Individual data points are shown as open black circles and means as coloured dots. The error bars show the SD.

Figure 7. *V. parvula* OM proteins other than OmpM paralogues are unlikely to be general diffusion channels. a AlphaFold2[45] models of the FNLLGLLA_00518 (OmpA-like) and FNLLGLLA_00833 proteins. The colours represent the per residue confidence of the prediction (pLDDT). **b** Molecular surface models of *V. parvula* OM proteins and EcOmpF as viewed from outside the cell. **c** Comparative liposome swelling assays with FNLLGLLA_00518 β-barrel, VpOmpM1 β-barrel, and EcOmpF. Each condition was measured in technical triplicates from the same proteoliposome preparation. Bars show mean ± SD.

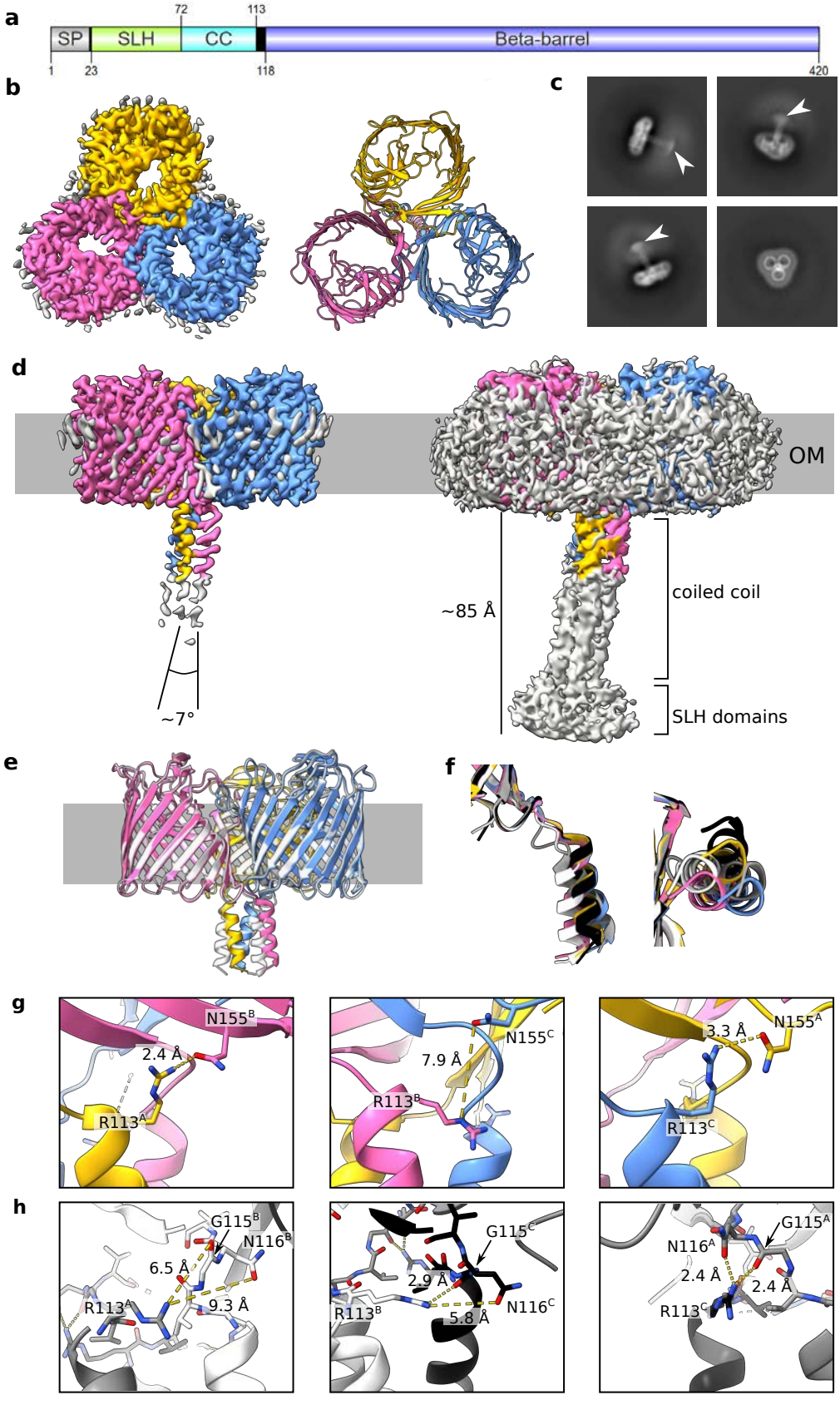
a
SP
SLH
CC
Beta-barrel
1
23
72
113
118
420
b
c
d
OM
~85 Å
coiled coil
SLH domains
~7°
e
f
g
N155B
2.4 Å
R113A
N155C
7.9 Å
R113B
3.3 Å
N155A
R113C
h
G115B
N116B
6.5 Å
9.3 Å
R113A
G115C
2.9 Å
R113B
5.8 Å
N116C
G115A
N116A
2.4 Å
2.4 Å
R113C

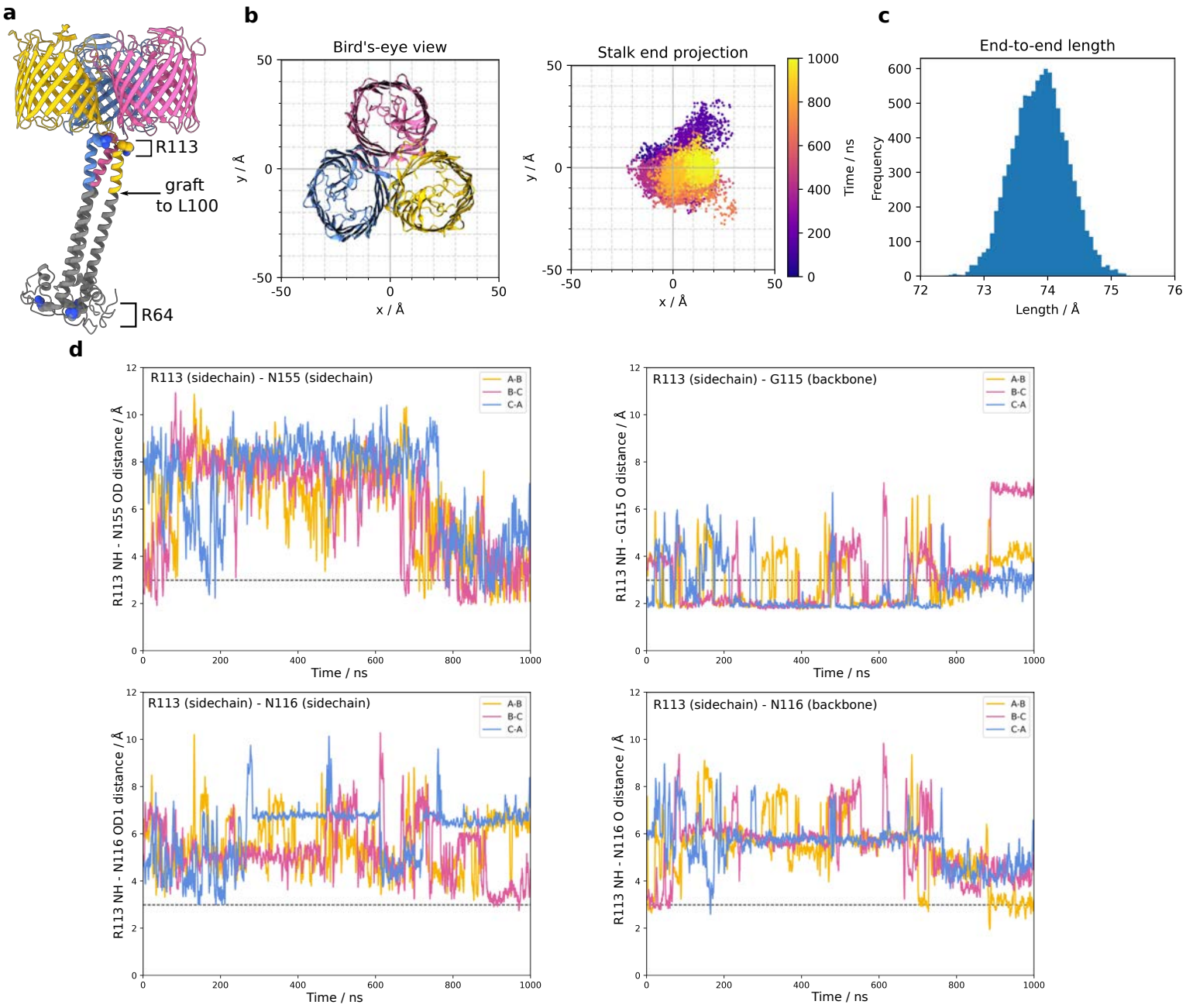
a
R113
graft
to L100
R64
b
Bird's-eye view
y / Å
x / Å
Stalk end projection
Time / ns
c
End-to-end length
Frequency
Length / Å
d
R113 (sidechain) - N155 (sidechain)
R113 NH - N155 OD distance / Å
R113 (sidechain) - G115 (backbone)
R113 NH - G115 O distance / Å
R113 (sidechain) - N116 (sidechain)
R113 NH - N116 OD1 distance / Å
R113 (sidechain) - N116 (backbone)
R113 NH - N116 O distance / Å
A-B
B-C
C-A
Time / ns

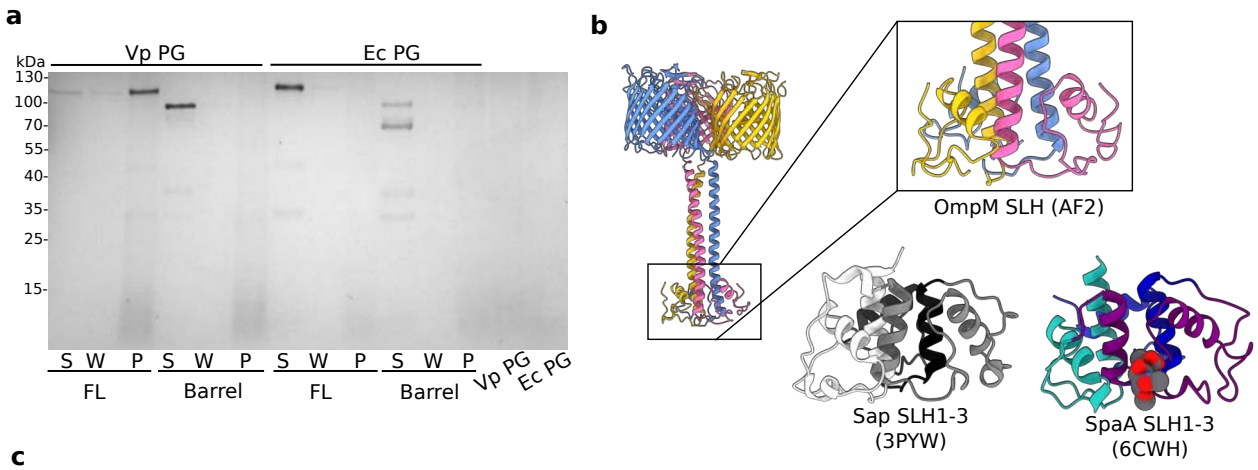
a
Vp PG
Ec PG
kDa
130-
100-
70-
55-
40-
35-
25-
15-
S W P S W P S W P S W P Vp PG Ec PG
FL
Barrel
FL
Barrel
b
OmpM SLH (AF2)
Sap SLH1-3
(3PYW)
SpaA SLH1-3
(6CWH)

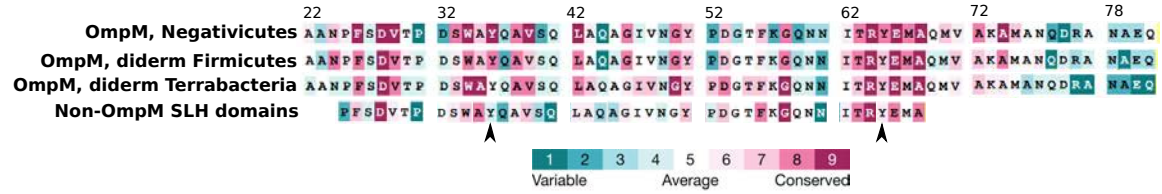
c
22
32
42
52
62
72
78
OmpM, Negativicutes
OmpM, diderm Firmicutes
OmpM, diderm Terrabacteria
Non-OmpM SLH domains
1 2 3 4 5 6 7 8 9
Variable
Average
Conserved

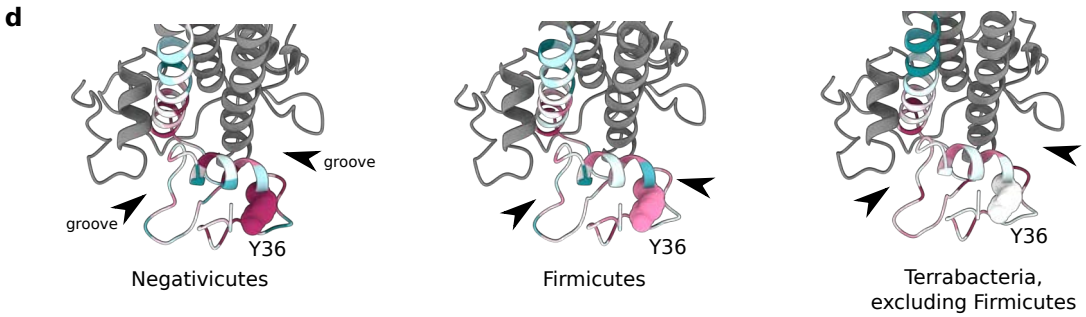
d
groove
groove
Y36
Negativicutes
Y36
Firmicutes
Y36
Terrabacteria,
excluding Firmicutes

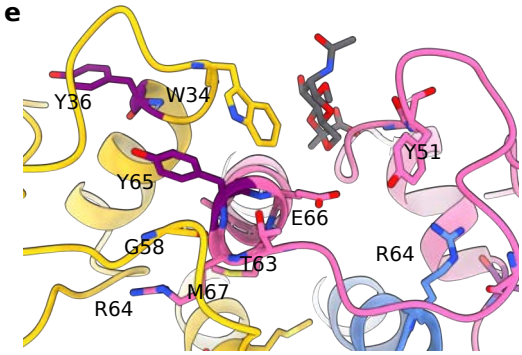
e
Y36
W34
Y51
Y65
E66
G58
T63
R64
M67
R64

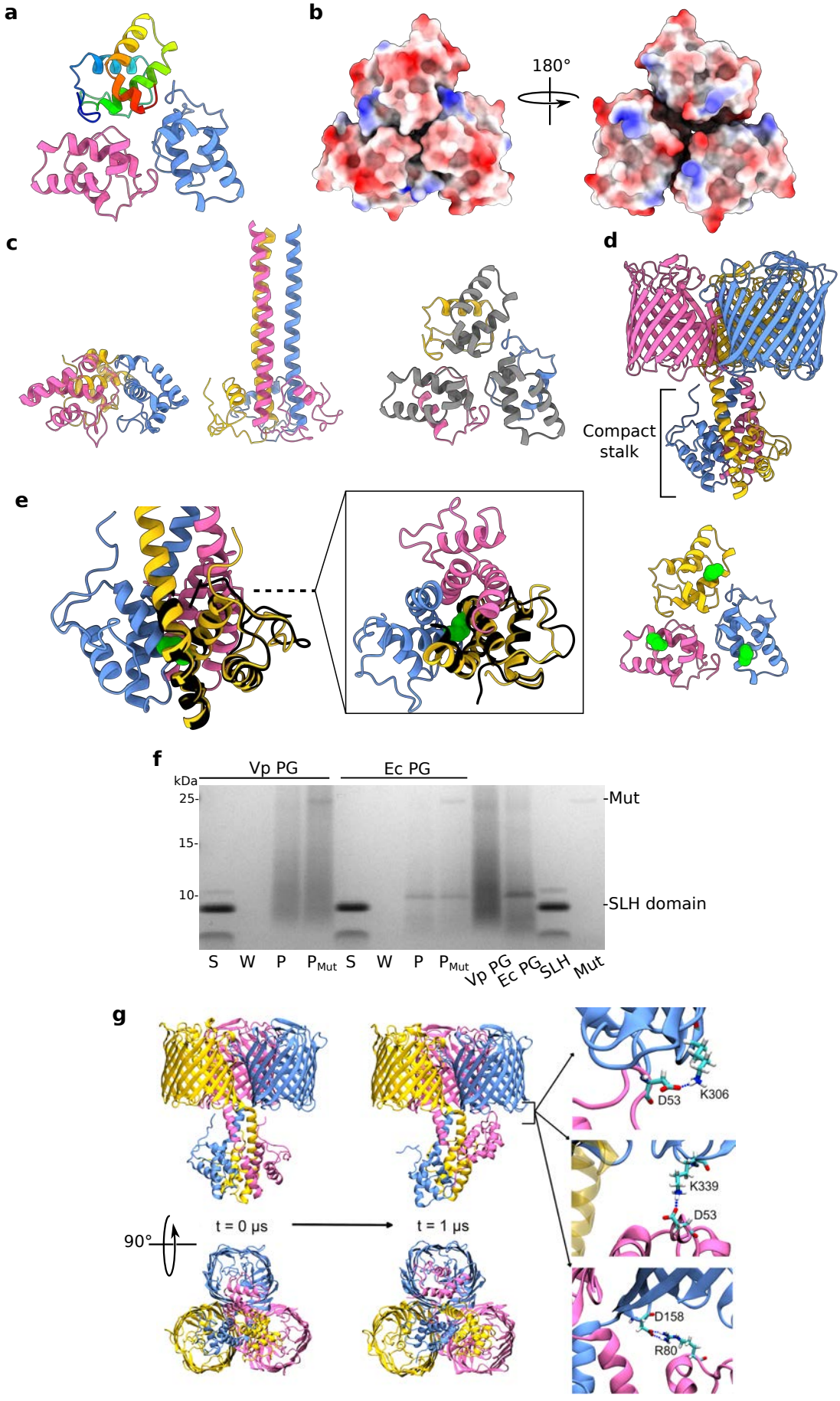
a
b
180°
c
d
Compact
stalk
e
f
Vp PG
Ec PG
kDa
25-
15-
10-
-Mut
-SLH domain
S W P P$_{Mut}$ S W P P$_{Mut}$ Vp PG Ec PG SLH Mut
g
90°
t = 0 µs
t = 1 µs
D53
K306
K339
D53
D158
R80

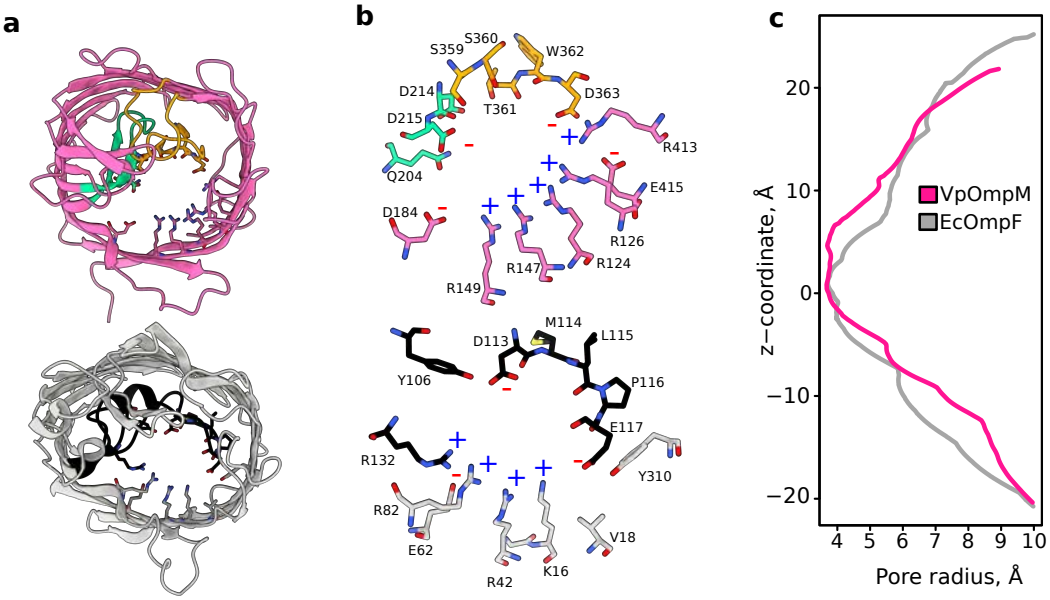
a
b
c
S359
S360
W362
D214
T361
D363
D215
R413
Q204
E415
D184
R126
R147
R124
R149
M114
D113
L115
Y106
P116
E117
R132
Y310
R82
V18
E62
R42
K16
20
10
0
−10
−20
4
5
6
7
8
9
10
z−coordinate, Å
Pore radius, Å
VpOmpM
EcOmpF

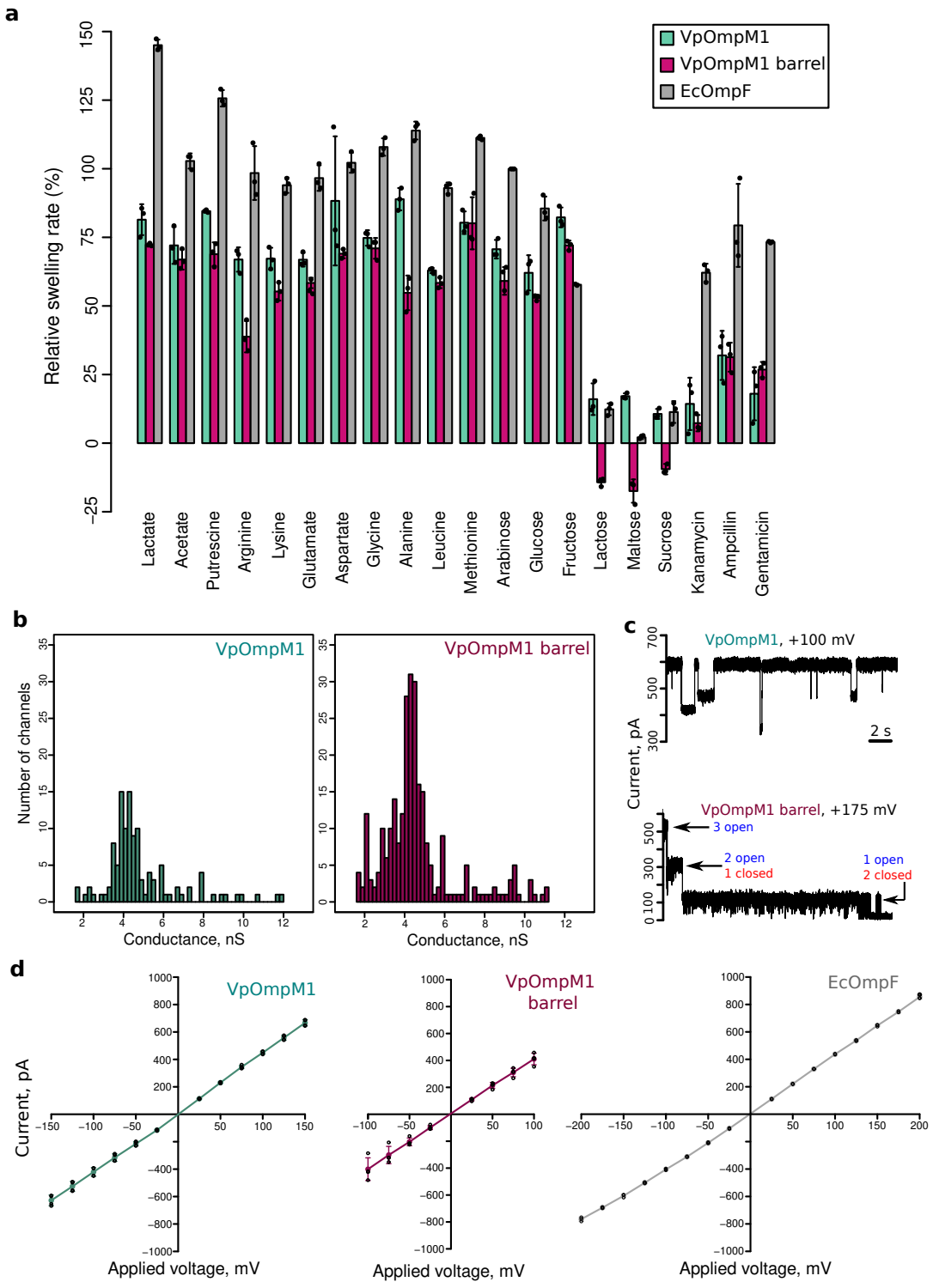
a
VpOmpM1
VpOmpM1 barrel
EcOmpF
Relative swelling rate (%)
Lactate
Acetate
Putrescine
Arginine
Lysine
Glutamate
Aspartate
Glycine
Alanine
Leucine
Methionine
Arabinose
Glucose
Fructose
Lactose
Maltose
Sucrose
Kanamycin
Ampcillin
Gentamicin
b
VpOmpM1
VpOmpM1 barrel
Number of channels
Conductance, nS
c
VpOmpM1, +100 mV
Current, pA
2 s
VpOmpM1 barrel, +175 mV
3 open
2 open
1 closed
1 open
2 closed
d
VpOmpM1
VpOmpM1 barrel
EcOmpF
Current, pA
Applied voltage, mV

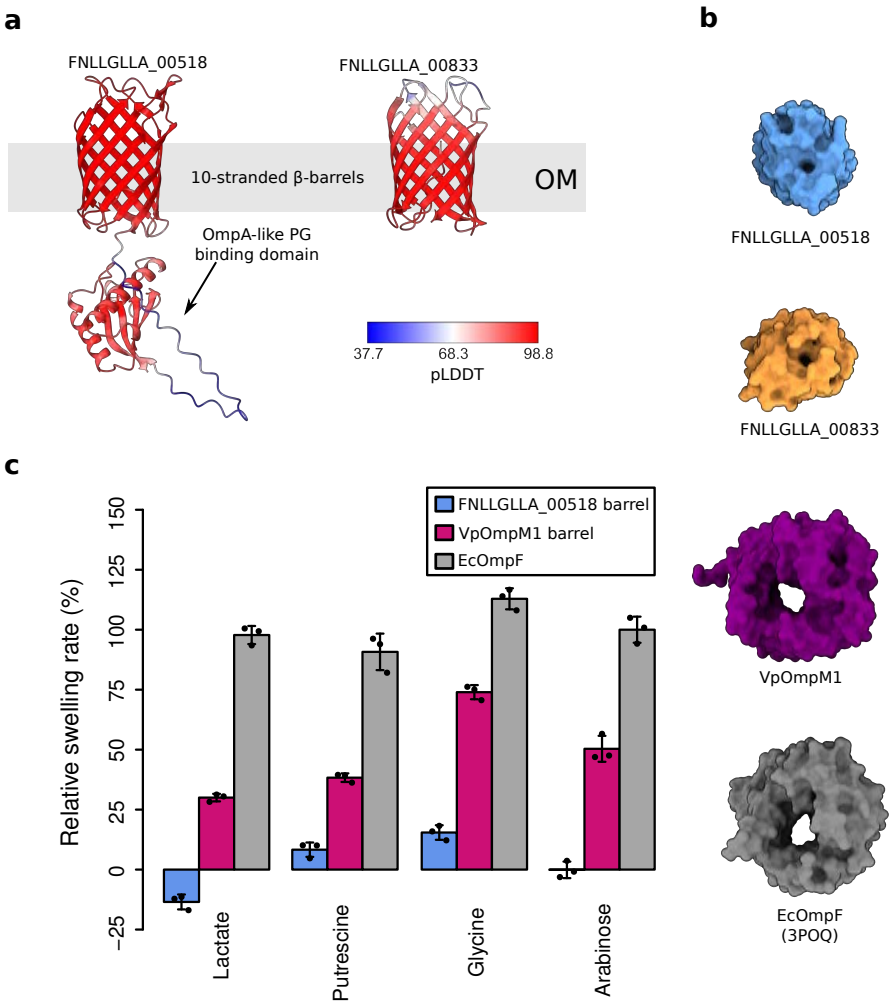
a
FNLLGLLA_00518
FNLLGLLA_00833
10-stranded β-barrels
OM
OmpA-like PG
binding domain
37.7
68.3
98.8
pLDDT
b
FNLLGLLA_00518
FNLLGLLA_00833
c
FNLLGLLA_00518 barrel
VpOmpM1 barrel
EcOmpF
Relative swelling rate (%)
−25
0
25
50
75
100
125
150
Lactate
Putrescine
Glycine
Arabinose
VpOmpM1
EcOmpF
(3POQ)

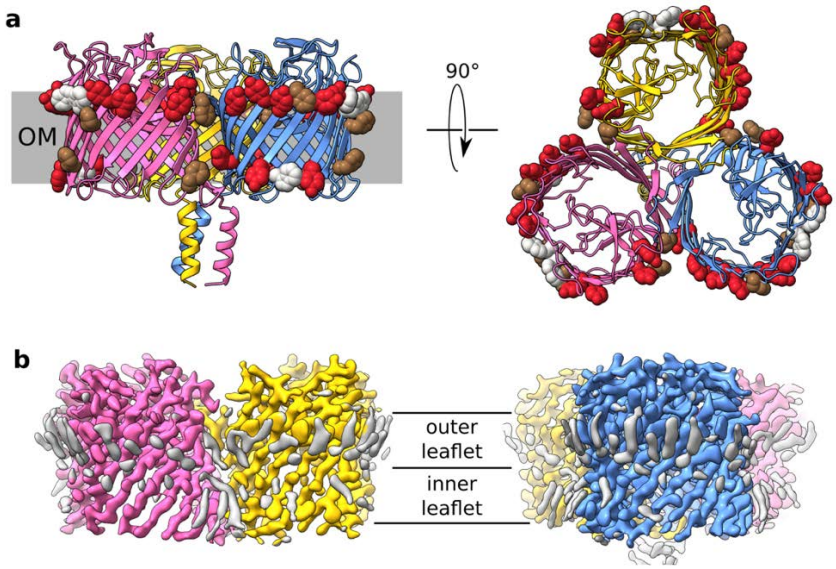

Supplementary Figure 1. VpOmpM1 aromatic girdle and putative lipid density. a Aromatic residues forming the aromatic girdle shown in space-filling representation on the cartoon of C1 VpOmpM1 reconstruction. Brown, phenylalanine; red, tyrosine; grey, tryptophan. **b** Cryo-EM density of the C3 VpOmpM1 reconstruction. Protein density coloured by chain; grey, putative lipid or detergent density.

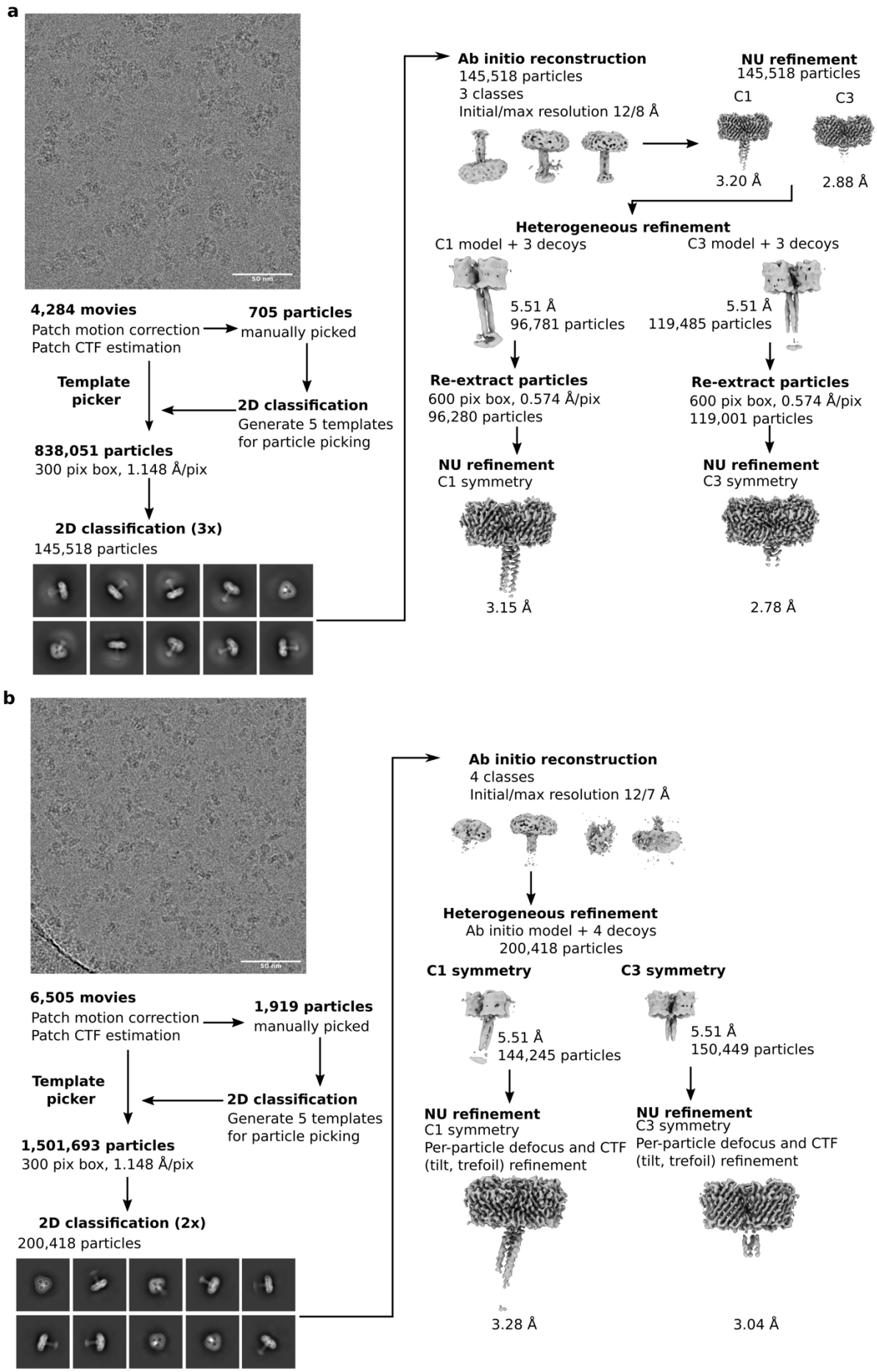

Supplementary Figure 2. Cryo-EM data processing. Cryo-EM data processing workflows for VpOmpM1 expressed in *E. coli* (**a**) and purified from *V. parvula* (**b**), showing representative motion-corrected movies, 2D class averages, and intermediate and final cryo-EM maps. A total of 4,284 and 6,505 movies were collected of grids with VpOmpM1 expressed in *E. coli* and *V. parvula*, respectively.

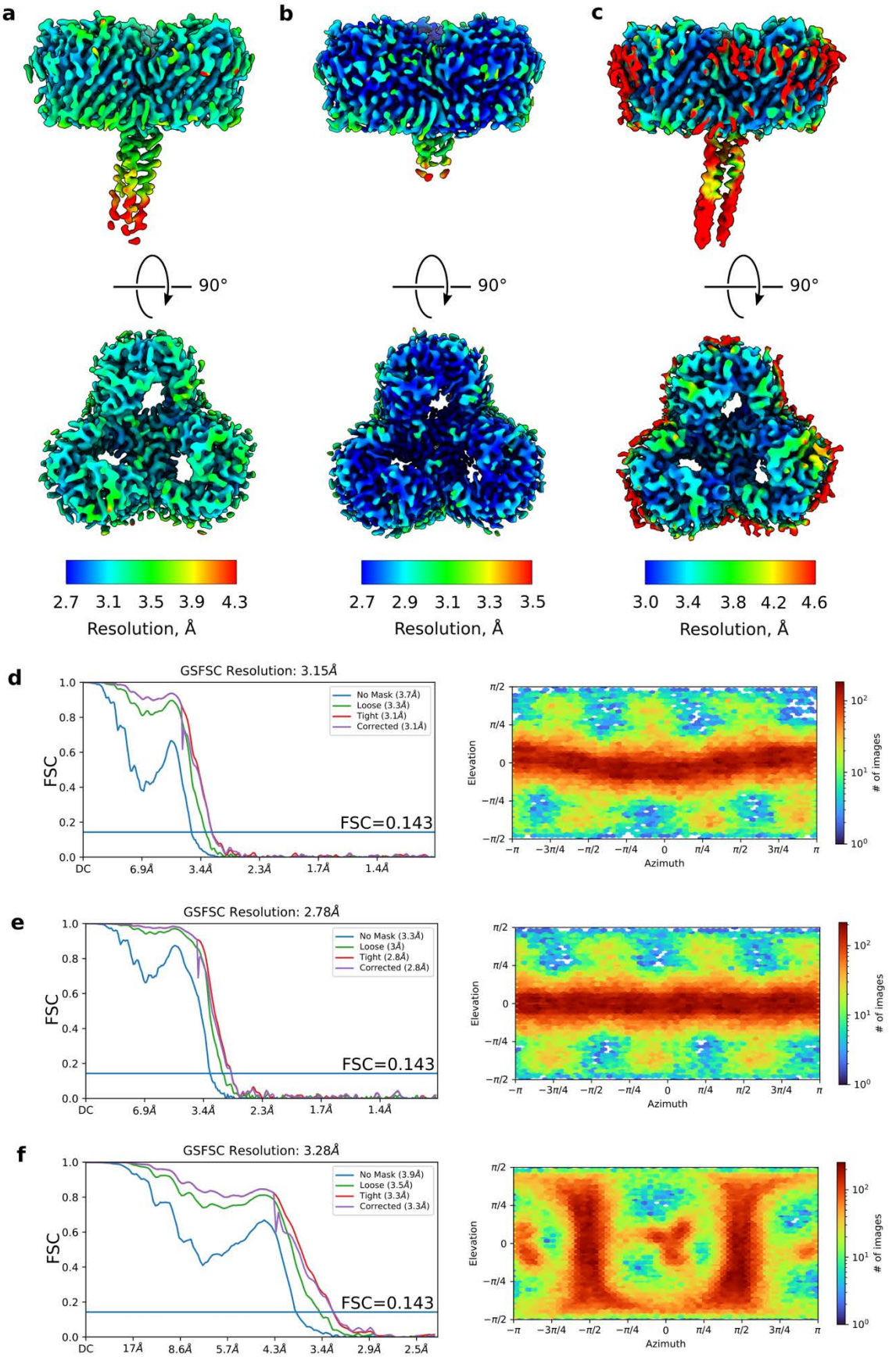

Supplementary Figure 3. Cryo-EM map local resolution estimates, FSC curves, and angular distribution plots. **a**, **d** VpOmpM1 purified from *E. coli*, C1 symmetry. **b**, **e** VpOmpM1 purified from *E. coli*, C3 symmetry. **c**, **f** VpOmpM1 purified from *V. parvula*, C1 symmetry.

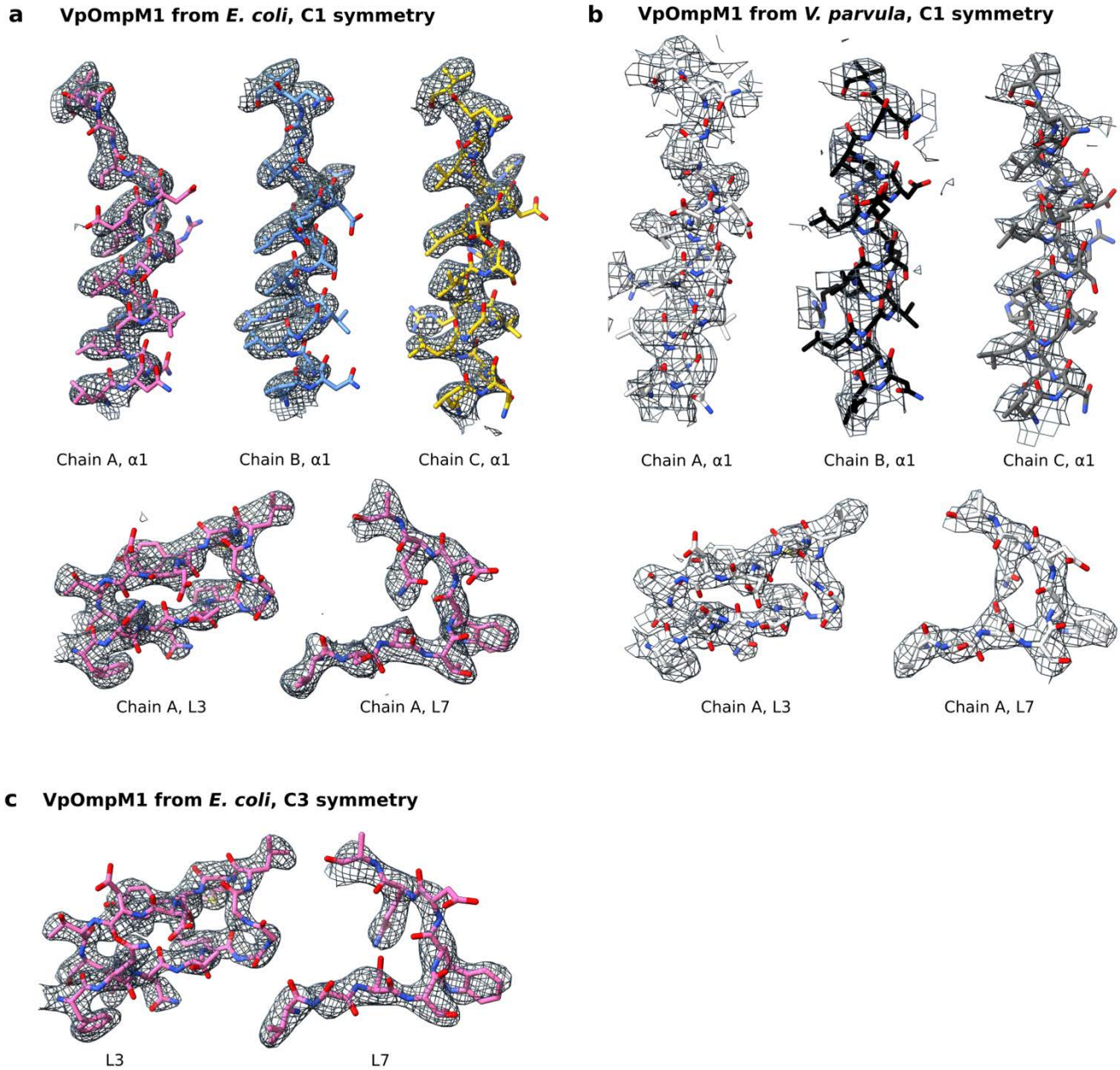

Supplementary Figure 4. Cryo-EM representative map-to-model fits. Densities and models for the stalk coiled-coil helix for each protomer and the eyelet loops 3 and 7 from a single protomer are shown for VpOmpM1 purified from *E. coli* (**a**) and from *V. parvula* (**b**) in C1 symmetry. Only the eyelet model fit for VpOmpM1 purified from *E. coli* with applied C3 symmetry is shown (**c**), as it was not possible to build a model into the stalk density in the symmetrized map. Protein models are shown in stick representation. Cryo-EM density is represented by a mesh.

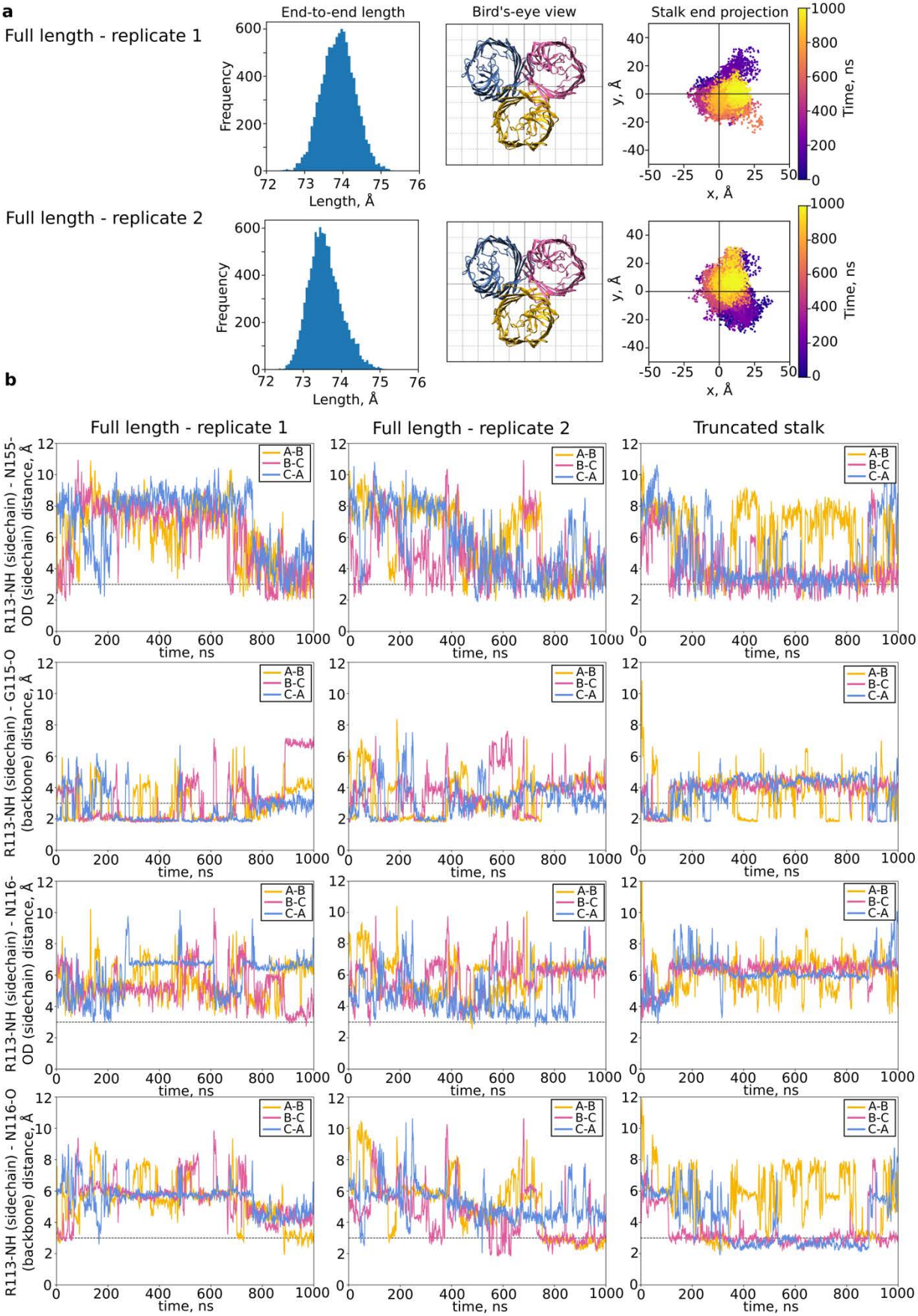

Supplementary Figure 5. All-atom molecular dynamics simulation replicates. **a** Stalk length and end projection plots for the two replicates of all-atom simulations with the native VpOmpM1 and AlphaFold2 graft model (full-length). The bird's-eye view coordinates correspond to the plot coordinates in the stalk projection plot. **b** Hydrogen bond distances throughout the simulation. The 'truncated stalk' simulation was performed with the native VpOmpM1 model without the AlphaFold2 graft. Data for replicate 1 shown in this figure are the same as the data shown in Figure 2.

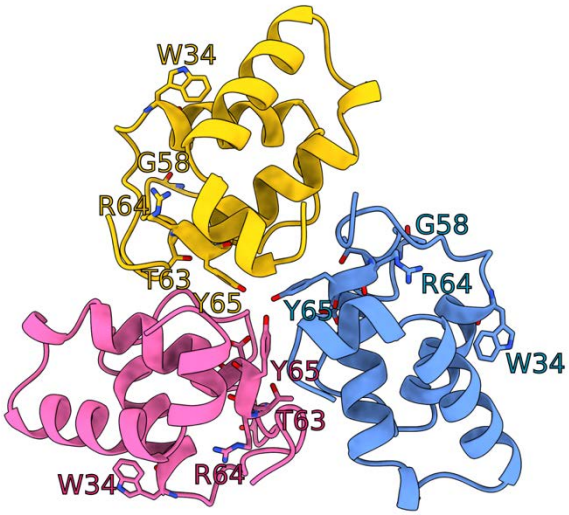

Supplementary Figure 6. Putative PG-binding motifs in the SLH crystal structure. Residues that are part of motifs conserved in SLH domains are shown in stick representation. Motif residues are not located in intra-protomer grooves as seen in crystal structures of SLH domains from monoderm Firmicutes and in the extended conformation of the VpOmpM1 stalk predicted by AlphaFold2 (Figure 3).

Rank	Chain	Z	rmsd	lali	nres	%id	Description
1	5f7l-C	5.7	2.5	57	375	11	Blood group antigen binding adhesin BabA
2	6bml-B	5.2	3.3	67	294	12	Human palmitoyltransferase DHHC20
3	6fws-B	5.2	3.3	68	683	4	Helicase DinG
4	6gmm-A	5.2	2.9	61	433	11	Adhesin LabA
5	6fws-A	5.0	2.7	65	686	8	Helicase DinG
6	7khm-A	4.8	3.3	68	290	12	Human palmitoyltransferase DHHC20
7	5f7w-A	4.8	2.7	60	419	10	Blood group antigen binding adhesin BabA
8	5f7y-A	4.8	3.2	62	417	10	Blood group antigen binding adhesin BabA
9	5has-A	4.7	3.2	64	381	5	DCB-HUS domain of Sec7
10	5f8q-A	4.7	2.4	56	419	11	Blood group antigen binding adhesin BabA

Supplementary Figure 7. SLH domain crystal structure DALI search results. DALI[1] analysis shows that the VpOmpM1 SLH domain crystal structure (PDB 8BZ2) has low similarity to other proteins from the PDB.

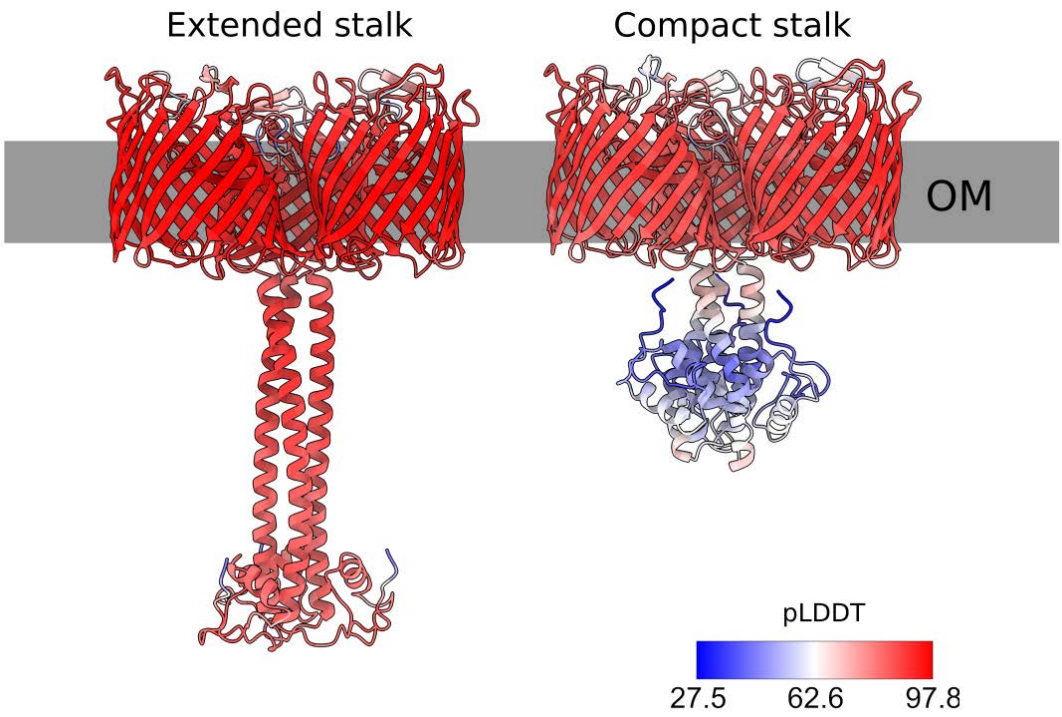

Supplementary Figure 8. VpOmpM1 trimer AlphaFold2[2] predictions. Cartoons coloured by per residue confidence score (colour key): pLDDT>90 – very high; 90>pLDDT>70 confident; 70>pLDDT>50 low; pLDDT<50 – very low.

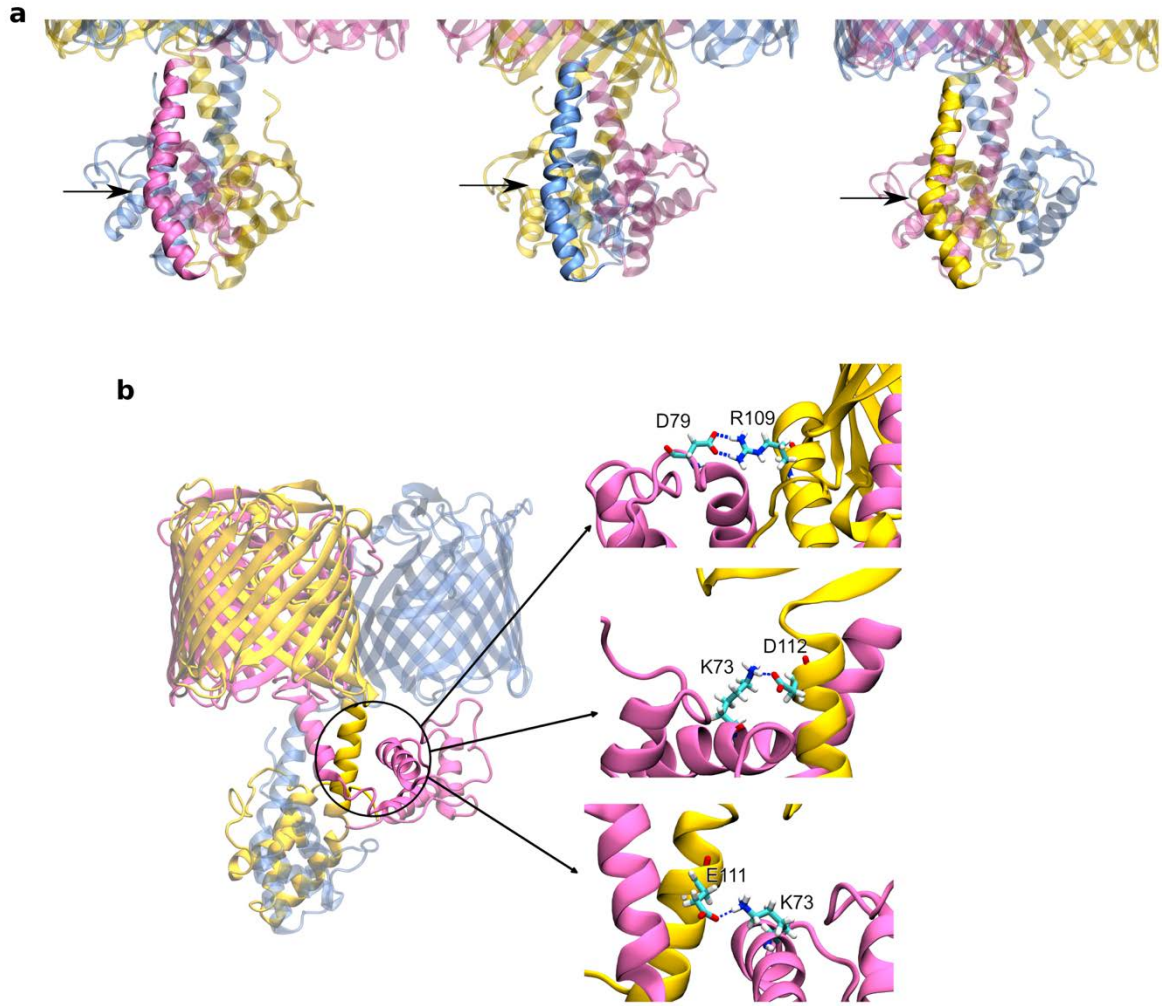

Supplementary Figure 9. VpOmpM1 compact stalk simulation. **a** The stalk α–helices in each protomer are kinked at residues 97-102 (arrows). This kink is the hinge that allows movement of the stalk towards the OM, as seen for the pink protomer in the simulation. **b** The conformation of the pink protomer is stabilised by salt bridge formation with the stalk of the yellow protomer. Salt bridge occupancy throughout the simulation (top to bottom): 14.33%, 3.21% and 1.27%.

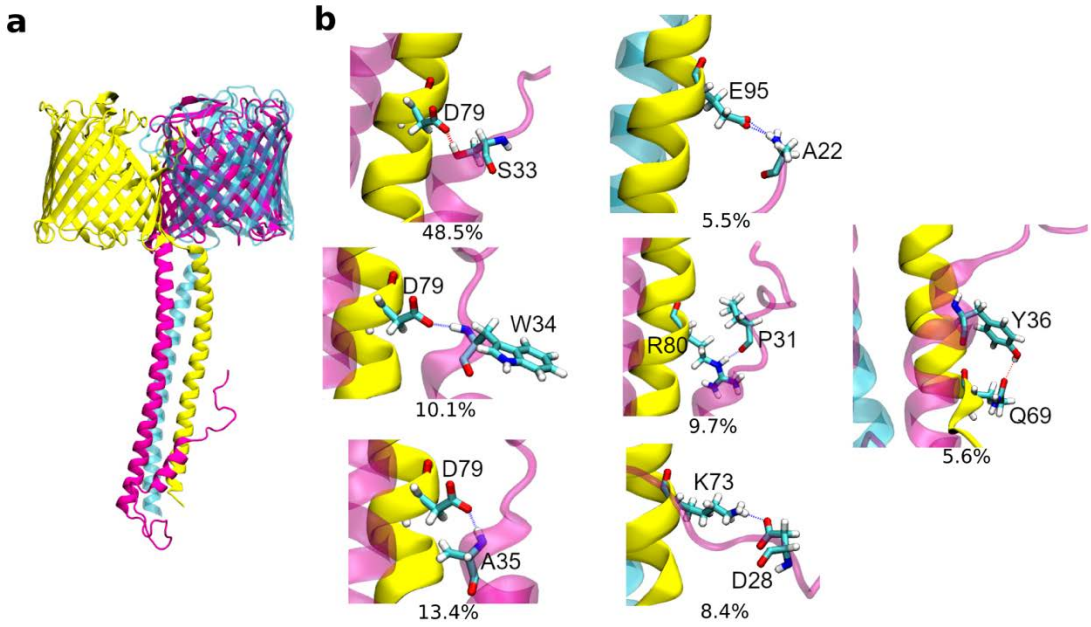

Supplementary Figure 10. Interaction of SLH domain with coiled-coil during extended stalk MD simulations. a During one all-atom simulation of VpOmpM1 with the grafted stalk, the SLH domain of one protomer (pink) unfolded and formed contacts with the coiled-coil region of another protomer (yellow). The SLH domains of the yellow and cyan protomers are not shown for clarity. **b** Close-up views of the SLH-coiled coil interactions. The percentage occupancy of each interaction throughout the 1 μs simulation is shown under each panel.

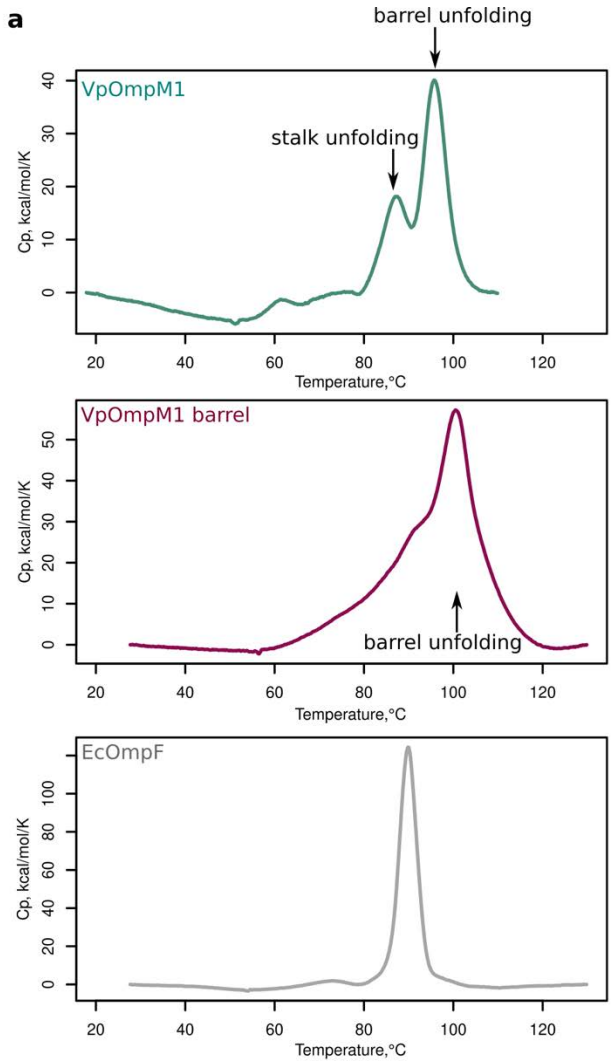

b

Sample	Melting temperature	
	T_m1	T_m2
VpOmpM1	87.46°C	95.74°C
VpOmpM1 barrel	92.27°C	101.06°C
EcOmpF	89.93°C	N/A

Supplementary Figure 11. Protein melting temperature analysis. **a** Dynamic scanning calorimetry thermograms for full-length VpOmpM1, VpOmpM1 barrel domain, and EcOmpF. Measurements were performed on a Malvern VP Capillary DSC instrument, using 18.7 μM protein in 10 mM HEPES-NaOH pH 7.0, 100 mM NaCl and 0.12% DM in each experiment. **b** Data were fitted and the melting temperatures (T_m) were extracted via the instrument manufacturer's software.

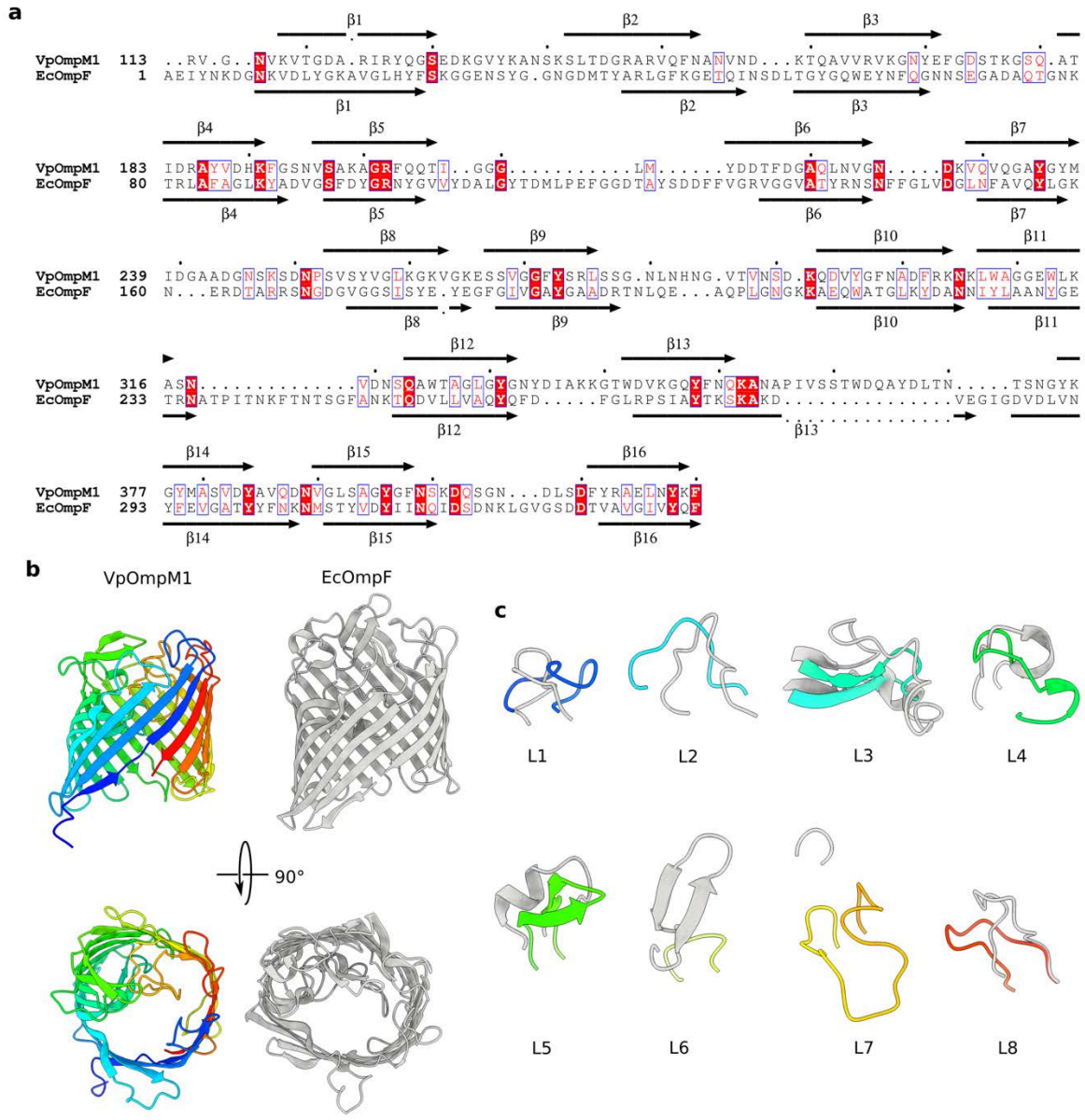

Supplementary Figure 12. Comparison of VpOmpM1 and EcOmpF. **a** Alignment of VpOmpM1 β-barrel and EcOmpF amino acid sequences. The alignment was generated by sequence-independent pairwise structure alignment of VpOmpM1 and EcOmpF (PDB 2ZFG) using TM-align[3] (RMSD 3.84 Å). Residues forming the barrel β-strands are annotated above and below the alignment for VpOmpM1 and EcOmpF, respectively. The sequences share 8% identity and 25% similarity. **b** Comparison of the VpOmpM1 β-barrel from C3 reconstruction (rainbow, N-terminus blue, C-terminus red) and EcOmpF (2ZFG; grey) structures. Views generated from a superposition. **c** Comparison of the extracellular loops (L1-8) of the two β-barrels as viewed from inside the β-barrel.

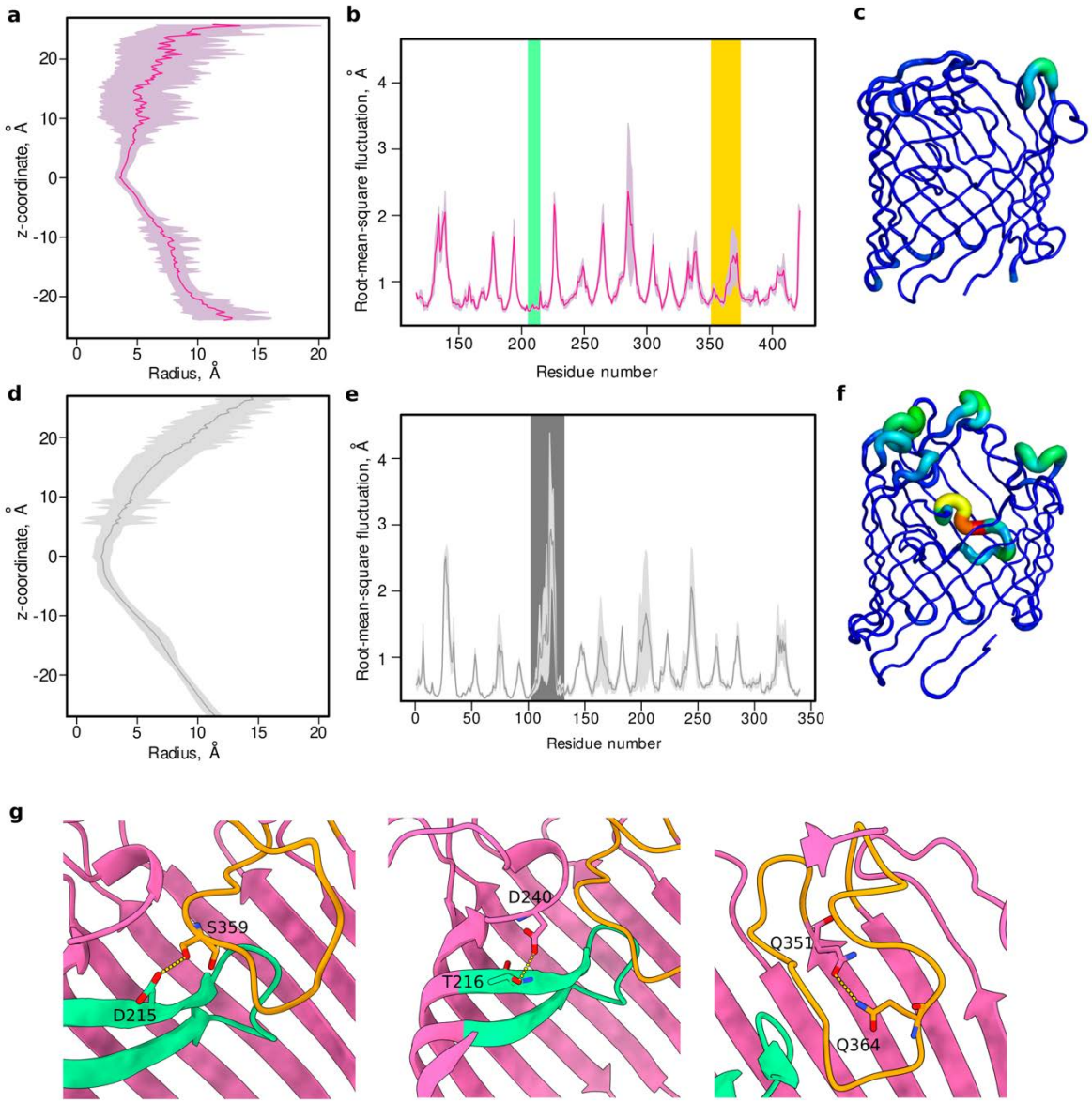

Supplementary Figure 13. Fluctuations in the channel regions of VpOmpM1 and EcOmpF during MD simulations. **a-f** Analysis of residue fluctuations in VpOmpM1 and EcOmpF during MD simulations. HOLE[4] analyses of VpOmpM1 (**a**) and EcOmpF (**d**) calculated averaged from all-atom MD simulation frames: 1 frame every 10 ns over the final 100 ns from 3 simulations, averaged over the 3 protomers (VpOmpM1, n=90 traces); 1 frame every 10 ns over the final 300 ns of a single all-atom simulation, averaged over the three protomers (EcOmpF, n=90 traces). Lines show the average values ± S.D. depicted by the shaded area. **b, e** Per-residue root-mean-square fluctuation (RMSF) plots for VpOmpM1 (**b**) and EcOmpF (**e**) during MD simulations. Same sampling as in **a** and **d**. Lines show the average values ± S.D. depicted by the shaded area. Residues forming the constriction loops are highlighted: VpOmpM1 L3, green; VpOmpM1 L7, orange; EcOmpF L3, grey. **c, f** Per-residue RMSF values converted to B-factors and displayed on VpOmpM1 (**c**) and EcOmpF (**f**) structures on the same scale. Cartoon thickness and colour (blue to red) are proportional to B-factor value. **g** Examples of interactions observed during simulations that likely restrict movement of the eyelet-forming loops of VpOmpM1: between the L3 and L7 loops (left), between L3 and L4 (middle), and between L7 and the internal barrel wall (right).

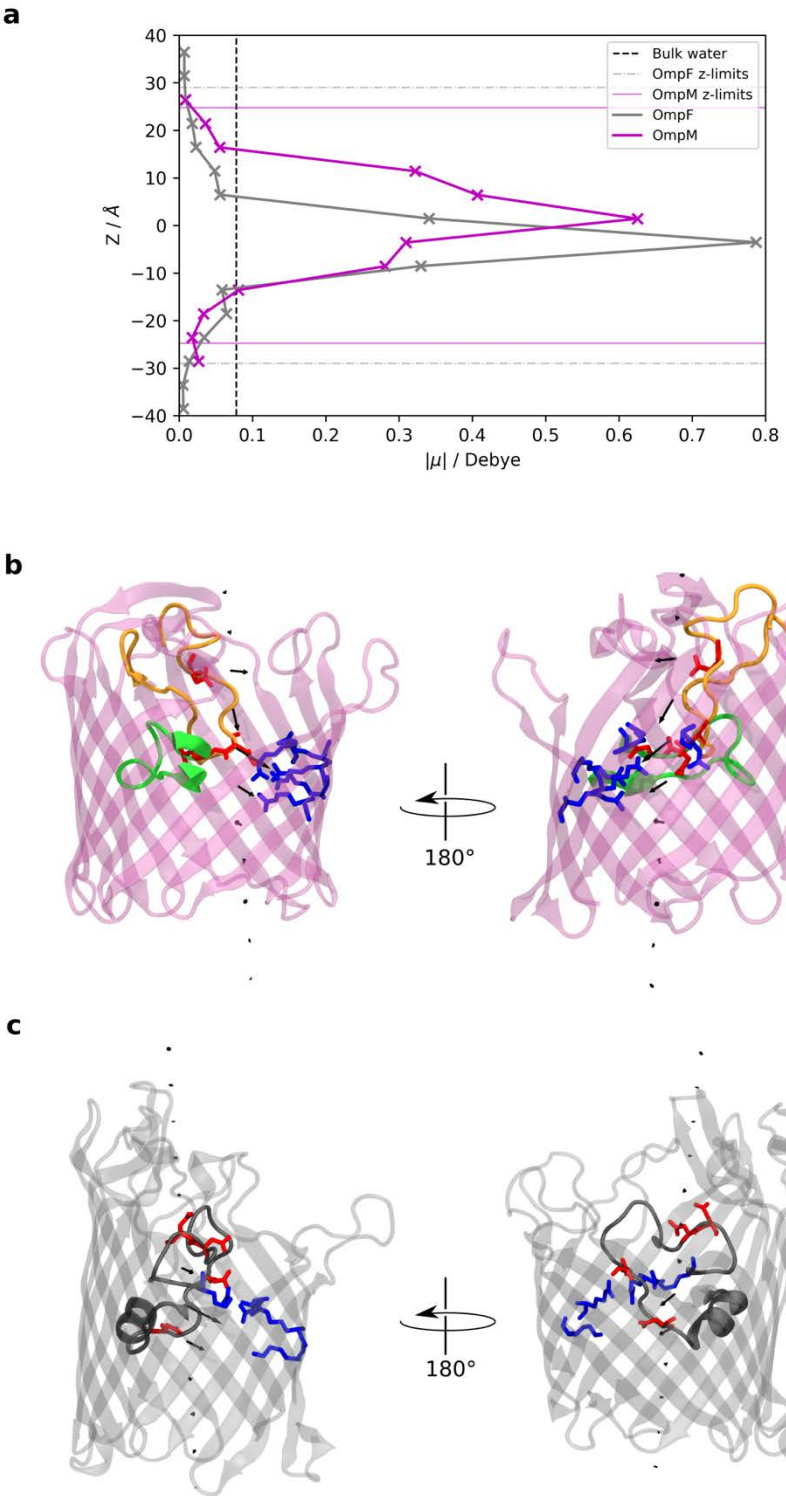

Supplementary Figure 14. Transverse electric field properties in VpOmpM1 and EcOmpF channels. **a** Total water dipole moment by z-coordinate, normalised to the number of water molecules in each z-slice. **b, c** Arrows indicate the direction of the dipole moment averaged across the waters in a particular z-slice over the final 100 ns of equilibrium simulations for VpOmpM1 (**b**) and EcOmpF (**c**). The length of the arrow is proportional to the magnitude of the dipole moment. VpOmpM1 loop 3 is green and loop 7 is orange; EcOmpF loop 3 is black. Basic loop residues are in blue and acidic residues are in red.

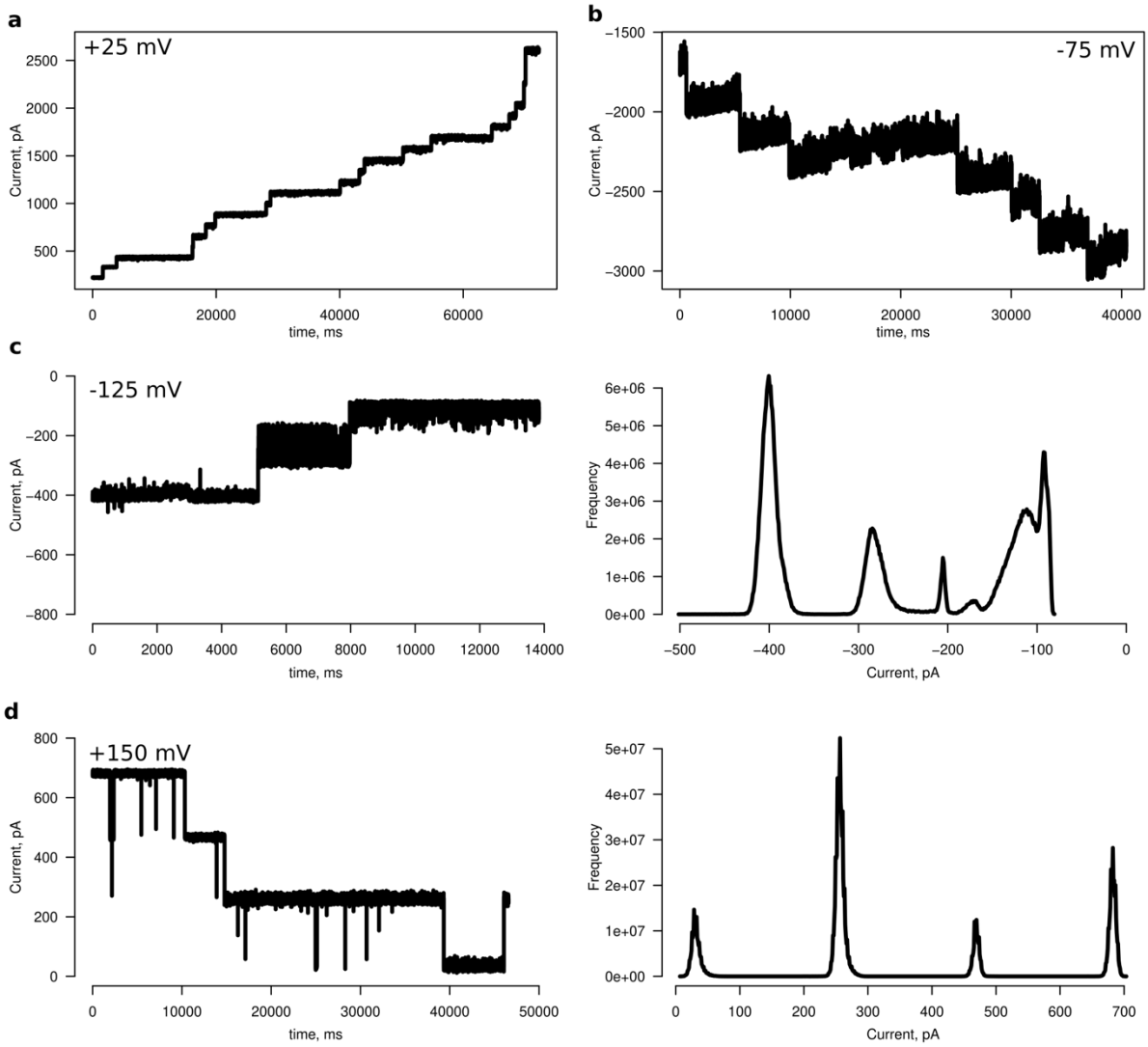

Supplementary Figure 15. Representative electrophysiology recordings. **a, b** Representative ion-current traces of full-length VpOmpM1 (**a**) and the barrel-only construct (**b**) showing multiple channel insertion events observed as 'steps' or sudden increases in current. **c, d** Ion-current traces for full-length VpOmpM1 (**c**) and the barrel-only construct (**d**) showing channel gating activity at high potential (left), with the corresponding all-current point histograms shown on the right. A 2.5 kHz low-pass eight-pole Bessel filter was applied to all traces. The applied voltage is indicated on each trace.

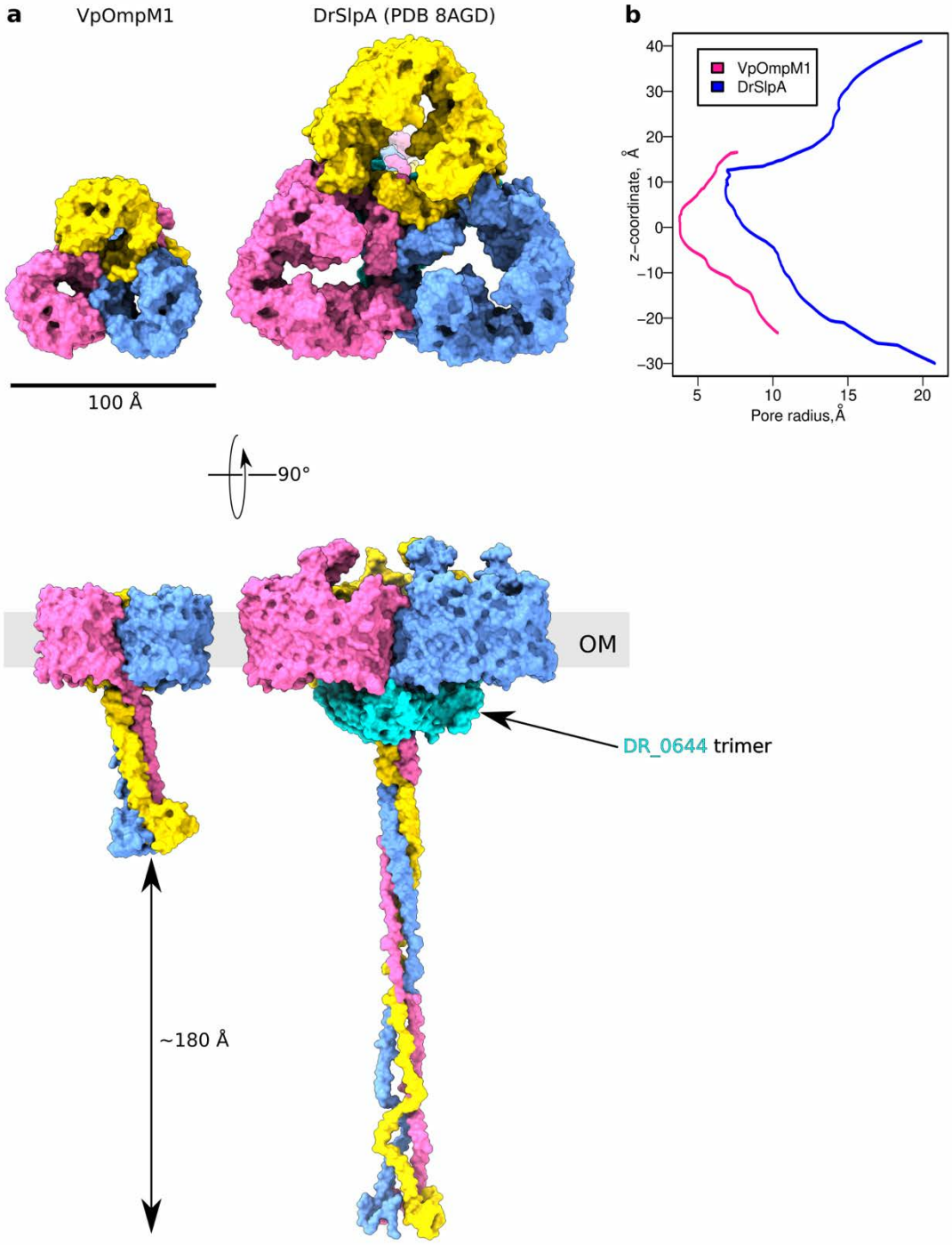

Supplementary Figure 16. Comparison of VpOmpM1 and DrSlpA structures. **a** To-scale surface representations of VpOmpM1 and *Deinococcus radiodurans* SlpA (DrSlpA) (PDB 8AGD[5]) from outside the cell (top) and from the OM plane (bottom). **b** HOLE[4] profiles of VpOmpM1 and DrSlpA. Note that the profiles show the path of a ball-shaped probe via the narrowest part of the pore and, therefore, this analysis grossly underestimates the size of the SlpA pore, since the constriction is not roughly circular as in VpOmpM1.

Supplementary Table 1. Cryo-EM data collection, processing and refinement statistics.

	VpOmpM1 from *E. coli*		**VpOmpM1 from *V. parvula***
Data collection			
Electron microscope	FEI Glacios		FEI Glacios
Voltage (kV)	200		200
Spherical aberration (µm)	2.7		2.7
Camera	Falcon 4 (counting)		Falcon 4 (counting)
Energy filter	none		none
Magnification	240,000		240,000
Pixel size (Å)	0.574		0.574
Total dose ($e^-/Å^2$)	50.1		50
Defocus minimum maximum (µm)	-1.0 to -2.0		-0.8 to -2.0
Number of movies collected	4,284		6,505
Image Processing			
Imposed symmetry	C1	C3	C1
Initial number of particles	838,051	838,051	1,501,693
Final number of particles	96,280	119,001	144,245
Global resolution (FSC = 0.143)	3.15	2.78	3.28
Map sharpening B-factor ($Å^2$)	-70.2	-85.5	-97.5
Refinement			
Model composition			
Non-hydrogen atoms	7,386	7,077	7,406
Protein residues	963	924	968
R.m.s. deviations			
Bonds lengths (Å)	0.003	0.002	0.004
Bond angles (°)	0.493	0.420	0.563
Validation			
MolProbity score	1.56	1.39	1.76
Clash score	4.52	3.57	6.45
Rotamer outliers (%)	0	0	0
Ramachandran plot			
Favoured (%)	95.30	96.41	93.97
Outliers (%)	0	0	0
PDB	8BYM	8BYT	8BYS
EMDB	EMD-16328	EMD-16333	EMD-16332

Supplementary Table 2. Crystallography data collection, processing and refinement parameters.

	VparOmpM1 stalk*
Data collection	
DLS beamline	I03
Wavelength	0.89842
Space Group	H3
Unit cell parameters	
a, b, c (Å)	118.71, 118.71, 47.24
α, β, γ (°)	90, 90, 120
Molecules in AU	3
Resolution range (Å)	34.78-1.57 (1.57-1.6)
I/σI	17.1 (0.7)
Completeness (%)	99.5 (92.9)
Multiplicity	9.0 (4.7)
Rpim (%)	1.7 (88.4)
$CC_{1/2}$ (%)	100 (23)
Phasing	
Ab initio	Arcimboldo[6]
Refinement	
Resolution (Å)	34.78-1.7
Rwork/Rfree (%)	21.9 /24.8
Reflections	
Non-hydrogen atoms	2,015
Protein only	1,918
Average B-factor ($Å^2$)	39.68
Rmsd	
Bond lengths (Å)	0.011
Bond angles (°)	1.21
MolProbity clashscore	3.75
Ramachandran plot	
Favoured (%)	99.59
Outliers (%)	0
PDB	8BZ2

*Statistics for the highest-resolution shell are shown in parentheses.

Supplementary Table 3. Bacterial strains used in this study.

Strain	Genotype	Reference or Source
***E. coli* DH5α**	*F- endA1 glnV44 thi-1 recA1 relA1 gyrA96 deoR nupG purB20* φ80d*lacZ*ΔM15 Δ(*lacZYA-argF*)U169, hsdR17($r_K^- m_K^+$), λ^-	Promega
***E. coli* TOP10**	*F- mcrA Δ(mrr-hsdRMS-mcrBC) φ80lacZΔM15 ΔlacX74 nupG recA1 araD139 Δ(ara-leu)7697 galE15 galK16 rpsL(StrR) endA1 λ-*	Invitrogen
***E. coli* BL21(DE3)**	*F- ompT lon hsdSB (rB- mB-) gal dcm* (DE3)	Invitrogen
E. coli* C43(DE3) *ΔcyoABCD	*F- ompT lon hsdSB (rB- mB-) gal dcm* (DE3) *lacUV5** ΔcyoABCD*	[7] (modified)
***E. coli* MFDpir**	*MG1655 RP4-2-Tc ::[Δmu1 ::aac(3)IV-ΔaphA-Δnic35-Δmu2 ::zeo] ΔdapA :erm-pir) ΔrecA*	[8]
***V. parvula* SKV38**	Wild type strain	[9]
V. parvula* SKV38 Δ*ompM1-3	*ΔFNLLGLLA_01389-7::tetM*	[10]

Supplementary Table 4. Plasmids used in this study.

Plasmid	Description	Reference or Source
pB22	pBAD22 vector with *E. coli* TamA signal sequence, N-terminal His_7-tag	[11,12]
pJW45	pB22 with beta barrel of *ompM1* cloned between XhoI and XbaI restriction sites	This study
pJW46	pB22 with *ompM1* (without signal peptide) CDS cloned between XhoI and XbaI restriction sites	This study
pJW48	pRPF185 with His-tagged *ompM1* (native RBS) cloned into the *Sac*I restriction site	This study
pRPF185	*Escherichia/Clostridium* shuttle conjugative expression vector with *tet* promoter	[13]
pBAD24	Vector for expressing proteins with their native signal sequence in *E. coli*	[11]
pBAD24-EcOmpF	pBAD24 vector with the full-length *E. coli* OmpF coding sequence cloned between EcoRI and XbaI restriction sites	This study
pET28b	*E. coli* expression vector	Novagen
pET28b-SLH_22-107	pET28b with *ompM1* SLH domain and stalk residues 22-107 coding region cloned between NcoI and XhoI sites (C-terminal His_6-tag)	This study
pB22-00518_21-200	pB22 with beta barrel (residues 21-200) of *FNLLGLLA_00528* cloned between XhoI and XbaI restriction sites	This study
pB22-00833	pB22 with beta barrel of *FNLLGLLA_00833* cloned between XhoI and XbaI restriction sites	This study

Supplementary Table 5. Primers* used in this study.

Primer	Sequence	Description
JW172	agcgttaacagatctgagcttaagaaagaaggaattcattatgaaaaaac	Forward primer for amplifying full length *ompM1* with its native RBS with homology arm to the pRPF185 digested with SacI
JW201	ccatcaccatcaccatcacctcgagcgcttggaagaccgtgtag	Forward primer for amplifying OmpM1 beta barrel with homology arm to the pB22 digested with XhoI
JW202	ctgaagcgggtgtgaatactctagattagaatttgtaatttaattctgcacg	Reverse primer for amplifying *ompM1* with homology arm to the pB22 digested with XbaI
JW203	ccatcaccatcaccatcacctcgaggctgcaaatccattctcc	Forward primer for amplifying *ompM1* without signal peptide with homology arm to the pB22 digested with XhoI
JW206	tctcctttactgcaggagct**ttaatgatgatgatgatgaccac c**gaatttgtaatttaattctgcacggtag	Reverse primer for amplifying *ompM1*, adding C-terminal 6His tag (indicated in bold) with homology arm to the pRPF185 digested with SacI.
00833_F	atactcgaggcatttgctgcagctcc	Forward primer for amplifying *FNLLGLLA_00833* without signal peptide with XhoI site
00833_R	atatctagattagaaggagtagcctacacc	Reverse primer for amplifying *FNLLGLLA_00833* without signal peptide with XbaI site
00518_F	atactcgagactcctcaaactcaattcaataaag	Forward primer for amplifying *FNLLGLLA_00518* barrel with XhoI site
00518_R	atatctagattaaccaccgaaacggtaagataatc	Reverse primer for amplifying *FNLLGLLA_00518* barrel with XbaI site
stalk_F	ataccatggctgcaaatccattctccg	Forward primer for amplifying *ompM1* stalk region with NcoI site
stalk_R	atactcgagctttacattacctacacggtc	Reverse primer for amplifying *ompM1* stalk region with XhoI site

* The part of the primer hybridizing to the template is indicated by an underscore.

Supplementary Table 6. Position restraints, timesteps (dt), and durations of the equilibration phases in the all-atom MD simulations.

Equilibration phase	Position restraint / kJ mol^{-1} nm^{-2}				dt/ fs	Duration / ns
	Protein Backbone	Protein Sidechains	Lipid Headgroups	Dihedrals		
NVT1	4000	2000	1000	1000	1	0.125
NVT2	2000	1000	400	400	1	0.125
NPT1	1000	500	400	200	2	0.5
NPT2	500	200	200	200	2	0.5
NPT3	200	50	40	100	2	0.5
NPT4	50	-	-	-	2	0.5

Supplementary Table 7. VpOmpM1 simulation composition.

System	Contents									Total atoms	Box dimensions, nm
	OmpM protomers	POPE	POPG	Cardiolipin	LPS	Potassium	Chloride	Calcium	TIP3P Water		
Truncated stalk (residue 100 onwards)	3	180	10	10	62	258	178	279	69,146	317,563	12.74 x 12.74 x 21.56
Full length extended stalk	3	162	9	9	55	324	241	247	91,443	377,626	12.22 x 12.22 x 27.40
Full length compacted stalk	3	162	9	9	56	268	185	252	71,804	319,677	12.25 x 12.25 x 23.18

Supplementary Table 8. EcOmpF simulation composition.

System	Contents									Total atoms	Box dimensions, nm
	OmpF protomers	POPE	POPG	Cardiolipin	LPS	Potassium	Chloride	Calcium	TIP3P Water		
EcOmpF	3	180	10	10	63	273	143	283	56,781	282,355	12.71 x 12.71 x 19.61

Supplementary Table 9. Substrate concentrations used in liposome swelling assays.

Substrate	Concentration (mM)
Figure 6 – VpOmpM1, VpOmpM1 barrel and EcOmpF	
Lactate	8
Acetate	8
Putrescine	8
Arginine	8
Lysine	8
Glutamate	10
Aspartate	8
Glycine	15
Alanine	15
Leucine	12
Methionine	15
Arabinose	12
Glucose	12
Fructose	12
Lactose	15
Maltose	15
Sucrose	15
Kanamycin	8
Ampicillin	8
Gentamicin	8
Figure 7 – FNLLGLLA_00518 barrel, VpOmpM1 barrel and EcOmpF	
Lactate	10
Putrescine	8
Glycine	15
Arabinose	10

Supplementary references

1. Holm, L. Dali server: structural unification of protein families. *Nucleic Acids Res.* **50**, W210–W215 (2022).
2. Jumper, J. *et al.* Highly accurate protein structure prediction with AlphaFold. *Nat. 2021 5967873* **596**, 583–589 (2021).
3. Zhang, Y. & Skolnick, J. TM-align: a protein structure alignment algorithm based on the TM-score. *Nucleic Acids Res.* **33**, 2302–2309 (2005).
4. Smart, O. S., Neduvelil, J. G., Wang, X., Wallace, B. A. & Sansom, M. S. P. HOLE: A program for the analysis of the pore dimensions of ion channel structural models. *J. Mol. Graph.* **14**, 354–360 (1996).
5. Farci, D., Graça, A. T., Iesu, L., de Sanctis, D. & Piano, D. The SDBC is active in quenching oxidative conditions and bridges the cell envelope layers in Deinococcus radiodurans. *J. Biol. Chem.* **299**, 102784 (2023).
6. Rodríguez, D. D. *et al.* Crystallographic ab initio protein structure solution below atomic resolution. *Nat. Methods 2009 69* **6**, 651–653 (2009).
7. Miroux, B. & Walker, J. E. Over-production of Proteins inEscherichia coli: Mutant Hosts that Allow Synthesis of some Membrane Proteins and Globular Proteins at High Levels. *J. Mol. Biol.* **260**, 289–298 (1996).
8. Ferrières, L. *et al.* Silent mischief: bacteriophage Mu insertions contaminate products of Escherichia coli random mutagenesis performed using suicidal transposon delivery plasmids mobilized by broad-host-range RP4 conjugative machinery. *J. Bacteriol.* **192**, 6418–6427 (2010).
9. Knapp, S. *et al.* Natural Competence Is Common among Clinical Isolates of Veillonella parvula and Is Useful for Genetic Manipulation of This Key Member of the Oral Microbiome. *Front. Cell. Infect. Microbiol.* **7**, (2017).
10. Witwinowski, J. *et al.* An ancient divide in outer membrane tethering systems in bacteria suggests a mechanism for the diderm-to-monoderm transition. *Nat. Microbiol.* **7**, 411–422 (2022).
11. Guzman, L. M., Belin, D., Carson, M. J. & Beckwith, J. Tight regulation, modulation, and high-level expression by vectors containing the arabinose PBAD promoter. *J. Bacteriol.* **177**, 4121–4130 (1995).
12. Van den Berg, B. *et al.* X-ray structure of a protein-conducting channel. *Nature* **427**, 36–44 (2004).
13. Fagan, R. P. & Fairweather, N. F. Clostridium difficile Has Two Parallel and Essential Sec Secretion Systems. *J. Biol. Chem.* **286**, 27483–27493 (2011).